City Research Online

City, University of London Institutional Repository

Citation: Khan, K., Chen, Z., Liu, J. & Tsavdaridis, K. D. (2023). Experimental and analytical investigations on compression behaviors of rotary-connected sway column-supported steel modular interior frames. Journal of Building Engineering, 78, 107692. doi: 10.1016/j.jobe.2023.107692

This is the accepted version of the paper.

This version of the publication may differ from the final published version.

Permanent repository link: https://openaccess.city.ac.uk/id/eprint/31222/

Link to published version: https://doi.org/10.1016/j.jobe.2023.107692

Copyright: City Research Online aims to make research outputs of City, University of London available to a wider audience. Copyright and Moral Rights remain with the author(s) and/or copyright holders. URLs from City Research Online may be freely distributed and linked to.

Reuse: Copies of full items can be used for personal research or study, educational, or not-for-profit purposes without prior permission or charge. Provided that the authors, title and full bibliographic details are credited, a hyperlink and/or URL is given for the original metadata page and the content is not changed in any way.

City Research Online: http://openaccess.city.ac.uk/ publications@city.ac.uk

Experimental and analytical investigations on compression behaviors of rotary-connected sway column-supported steel modular interior frames

Kashan Khan[a], Zhihua Chen[a,b,c], Jiadi Liu[a], Konstantinos Daniel Tsavdaridis[d]

[a] *Department of Civil Engineering, Tianjin University, Tianjin, China*

[b] *State Key Laboratory of Hydraulic Engineering Simulation and Safety, Tianjin, China*

[c] *Key Laboratory of Coast Civil Structure and Safety, Tianjin University, Tianjin, China*

[d] *School of Science & Technology, Department of Engineering, City, University of London (UK)*

Abstract: This study examines the compressive behaviors of sway column-supported steel modular interior frames (SCSMIFs) using rotary-type vertical and horizontal inter-modular connections (IMCs). The compression behavior of SCSMIFs was investigated through experimental, numerical parametric, and analytical techniques. Findings indicate that the relative rigidity of beam-to-column connections primarily influences lateral translation. Adjacent upper columns displayed symmetrically inward or outward elastic and plastic S-shaped local buckling without IMC failures. A finite element model (FEM) was developed and validated, achieving a 1% average prediction error for compressive resistance. The examination of 87 SCSMIFs with a validated FEM revealed the effects of different parameters on compressive resistance, initial stiffness, and pre-and post-ultimate ductility. Based on member stiffnesses and rotary-type IMCs in semi-rigid and pinned conditions, theoretical models predicted sub-assembled CMSIF buckling loads. The average theory-to-FEM results for pinned and semi-rigid IMCs were 0.70 and 0.95, indicating that incorporating the stiffness of rotary-type IMCs resulted in more accurate and less scattered buckling load predictions. Considering their unique characteristics, the study's findings contribute to ensuring the structural integrity and design of SCSMIFs with IMCs under compressive loads.

Keywords: Compression behaviors; Inter-modular connections; Column-supported frames; Sub-assembled testing; Finite element analysis; Buckling load models

1 Introduction

Modular steel buildings (MSBs) employ prefabricated volumetric modules as a practical, superior, secure, and sustainable alternative to conventional steel buildings. These modules are assembled with intra-modular connections (ITCs) and vertical and horizontal inter-modular connections (IMCs) [1,2]. Successful MSB applications, such as the 44-story Croydon, 32-story B2, and 29-story SOHO and Apex, highlight the practicality of these structures [3–5]. Compared to braced, hybrid, or wall-supported systems, column-supported steel modules offer simple connectivity, a distinct load transfer path, and high prefabrication levels [6,7]. The applications and benefits of these modules and MSBs were apparent when the first government-approved MSB in China was produced in just one month using 314 modules [2,8–10].

The structural performance of MSBs is mainly reliant on ITCs and IMCs, particularly vertical installation and horizontal connectivity. While welded ITCs [11–15] are preferred for beams and columns over bolted [16,17] or fin-plate [7] due to their increased resistance [2], IMCs transfer forces vertically and horizontally between modules and considerably influence structural stability, robustness, and behavior [18]. Thus, they have been the subject of extensive research, as reviewed in [4,5,19–23]. Recent literature has proposed varying reliable bolted [24–27], welded [11–15], shear-keyed [28–31], automatic [32–35], and pre-and post-tensioned [36–39] IMCs. A wealth of research has investigated IMCs' mechanical performances under various loadings. Shear loading research is summarized in [40–42], tensile in [33,40,43], bending in [9,44,45], and seismic in [46–48]. Despite this, calculating buckling length and load in frame columns subjected to compressive loads remains challenging. This is owing to the properties of IMCs, which include semi-rigidity and discontinuity, distinguishing IMCs from the semi-rigid joints of regular frame systems and affecting the structural rigidity, capacity, and resilience [49].

There has been extensive study on the compressive behavior of ordinary steel columns. Liu et al. [50] observed that reducing the width-to-thickness ratio improved the ductility and bearing capacity of the tube. Nie et al. [51] examined multiple dimensions, slenderness ratios, and eccentricities while applying eccentric compression to tubular columns. They discovered that the columns exhibited global buckle and significant lateral deflections. Fratamico et al. [52] revealed that most of the instability in duplex composite columns was caused by local buckling. While designing for compressive loads, stability demands are crucial for ensuring the structure's resistance to buckle and overall integrity [53]. Thus, stability design largely depends on the effective length factor, based on the degree of elastic restraint at the column's ends like in IS800 [54,55], NZS 3404[56], EC3:1-1 [57], CSA S16-19 [58], AISC360-16 [59], and GB 50017-2017 [60]. While these works provide valuable insights, these computations might not apply to the design of MSBs due to semi-rigid IMCs between columns, which alter the constraint conditions at both ends of the columns and consequently impact the buckling length, load and overall stability. Existing practices using alignment charts [61] and simplified equations [62] may result in the design of MSBs that are non-conservative, excessively conservative, economically inefficient, or inadequate, with engineers assuming substantial risks due to the unpredictability and variance of the behavior to conventional systems [63].

Despite the extensive research conducted on conventional columns, there are limited investigations on the compressive behavior of MSBs. Lawson et al. [64] addressed these issues with compressive tests on multi-column walls and a second-order analysis method integrating hypothesized horizontal forces for module column stability analysis. Hou et al. [65] and Khan et al. [66–68] investigated the buckling behavior of multi-column walls and discovered that concrete cladding reduced buckling and that GB50017 estimates were most reliable. Their research, however, assumed uniform load distribution across all columns and disregarded the effect of adjacent modular units, IMCs, and complex joint zones. Deng et al. [69], Chen et al. [70], and Khan et al. [71–73] carried out investigations on single and grouped columns with shear-keyed IMCs. They formulated theoretical buckling load equations and modified code predictions for conservative design. However, these studies assumed complete column-to-endplate welding, impractical for interior IMCs, or shear-keyed columns, which cannot design other columns and do not involve semi-rigid connections between adjacent modules. Zhang [74] established a simplified analysis model to calculate the column buckling length; however, this model was limited to single-story and single-module columns, and its relevance to the design of multi-story MSB columns requires further confirmation.

Further studies, including those conducted by Li et al. [75,76], Farajian et al. [49], Zhai et al. [77], and Wang and Su [78], examined stability calculations in sway and non-sway semi-rigid steel frames with corner connections using simplified modeling techniques. These studies developed alignment charts for columns *K*-factors and proposed simplified formulas following the French Rules [79]. However, these studies lacked experimental support for particular types of IMCs, missed to account for the rotational stiffness of vertical and horizontal inter-modular connection and joint design separately, relied on simplified formulas with limited data for fitting, and failed to account for variable story heights and varied height-to-span ratios. As these alignment charts rely on the designer's visual interpretation, they are also susceptible to error, indicating the need for more precise and straightforward approaches [77]. Besides, classification methods similar to those put forward by Farajian et al. [80,81] and He et al. [82] primarily characterize the response characteristics of connections regarding their strength and rotational stiffness. They provide design recommendations and validate their proposed systems but neglect further discussion on aspects such as non-linear analyses and the post-buckling behavior of structures under multiple limit states. The current practice calculates the buckling length and load for MSB as abnormal values because the actual structural mechanism cannot be correctly identified with simplified connections or modeling techniques [83]. Indeed, compressive tests must account for the *P*-delta effect, the relative stiffness of module members and IMCs, and the stiffness of vertical and horizontal IMCs to produce accurate FEMs and replicate the actual behavior of rotary-connected sway column-supported steel modular interior frames (SCSMIFs) [2,21,84–87]. Such analyses should then focus on the non-linear behavior of SCSMIFs. Consequently, a comprehensive approach featuring compressive testing, accurate modeling, analysis, and design of MSB is required to address these deficiencies and provide a conservative method employing equations to evaluate buckling load from semi-rigid to pinned boundaries, thereby eliminating the need for charts. Considering the compressive performance of these systems, specific types of IMCs [88], and the stability-relevant mechanical properties of IMCs [2], it is crucial to investigate global stability and reliable design methods in greater detail [83].

The present study intends to contribute to this field by investigating the compressive behavior of SCSMIF using rotary-type IMCs, as described in Ref. [9]. Two sub-assembled interior module frames were compressed as sway frames [88]. Validated FEMs explored the effects of varying parameters. Experimental and FEM data verified theoretical models assuming semi-rigid and pinned IMCs for predicting sub-assembled rotary-connected SCSMIF buckling loads to design cost-effective, secure, and sustainable MSBs.

2 Compression tests on rotary-connected SCSMIFs

Compressive behavior of rotary-connected SCSMIFs involves testing sub-assembled interior frames designed to represent the sway frame behavior.

2.1 Specimens design

As the engineering basis for the study's members and IMC designs, the selected prototype comprised the design of 8.5×3.0×3.0 and 6.7×3.0×3.0 m rotary-connected modules for the construction of 5-story Ziya Shanglinyuan MSBs [2,8–10,40,89]. The design was executed in compliance with GB50017-2017 [60]. Two sub-assembled interior frames with unique roller support on beam ends were designed to examine the compressive behavior and failure response of rotary-connected SCSMIF [88]. The testing was intended to investigate the compressive behavior and failure response of SCSMIFs, collect empirical data for FEM validation, and then carry out parametric and theoretical research to develop buckling load models utilizing rotary-type IMCs. The current investigation used sub-assembled specimens to achieve results comparable to those of full-frame studies [32,33,36,46,88,90,91]. Groove welding was used to create butt joints in the middle of the section of columns and beams. A gap of 74 mm was maintained between floor and ceiling beams, and a gap of 24 mm between adjacent columns, following the design of the prototype project to allow for access and installation of MEP facilities [88].

2.2 Specimens geometry

The assembly process of SCSMIFs featuring rotary-type IMCs followed Refs. [2,8–10,40,89]. The specimens' geometry, boundary configurations, and IMC details are illustrated in **Fig. 1(a~c)** and **Table 1**. Because of the primary load-bearing member, floor beams' flexural stiffness was kept higher than ceiling beams', resulting in floor beams (B_{FB}) having a deeper cross section than ceiling beams (B_{CB}). While RDD-2 selected identical thicknesses of 8 mm, RDD-1 opted for thicker floor beams (t_{FB}) of 8 mm and thinner ceiling beams (t_{CB}) of 6 mm [90]. In RDD-2, t_{CB} was raised to 8 mm. To analyze the impact of beam and ITCs' relative stiffness on the compressive properties of SCSMIF, different t_{FB} and t_{CB} were tested while ensuring consistency with the original prototype design. The IMC details and the members' cross-sectional sizes, columns height (L_c), and beam lengths (L_{FB} and L_{CB}) were kept unchanged. The sub-assemblage is recognized as a precise and standard approach for determining the height and length of members at the inflection point [88]. The specimens were created with consistent dimensions of 3375 mm in height and 3160 mm in width to satisfy design and laboratory specifications. The clear height and length of the upper and lower columns (L_c) were maintained at 1266 mm, while the floor (L_{FB}) and ceiling (L_{CB}) beams were kept at 1192 mm for both the left and right modules. The chosen column was a 200×200×8 mm size, with a length of 200 mm (D_c), width of 200 mm (B_c), and thickness of 8 mm (t_c). For the floor beams, a width (D_{FB}) and depth (B_{FB}) of 150 and 200 mm were utilized, while a width (D_{CB}) of 150 mm and depth (B_{CB}) of 150 mm were selected for the ceiling beams.

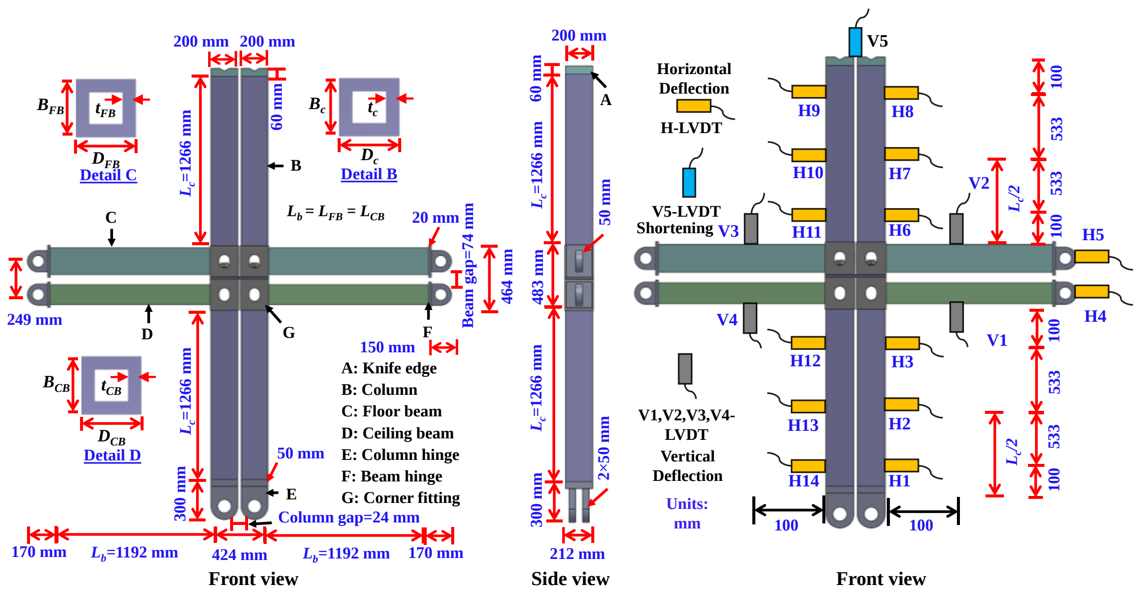

(a) Specimen geometry and LVDTs installation details

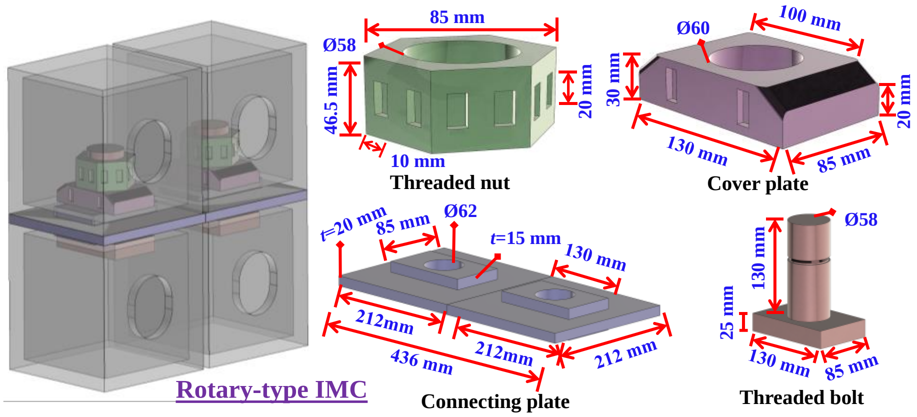

(b) Rotary-type IMC's components design details (Prototype & Tests)

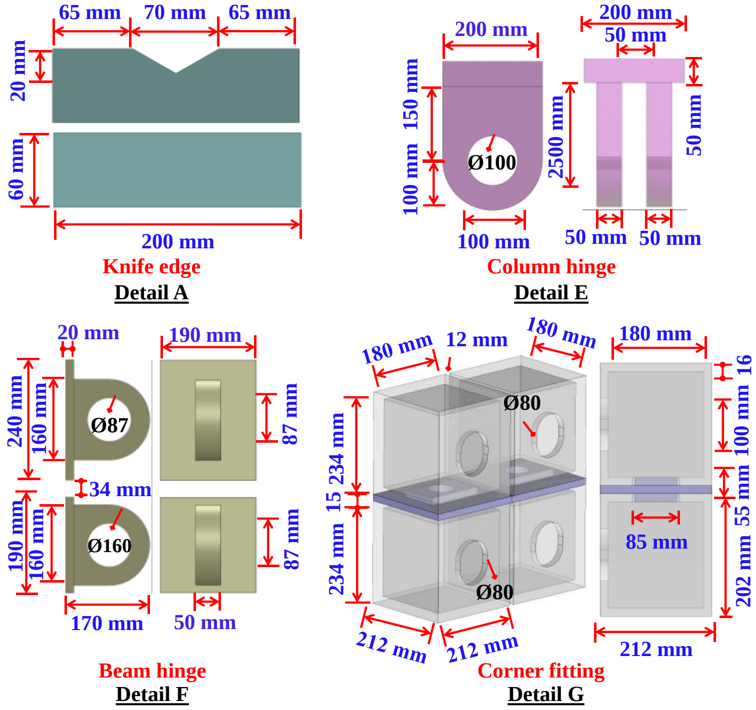

(c) Details of the selected components

Fig. 1 Details of tested sub-assembled rotary-connected SCSMIFs

2.3 Material properties

Steel coupons, made from the same material as the frames, were created following GB/T228.1-2010 [92] for analyzing test outcomes and generating FEM. Measurements of the thicknesses of 15 coupons, with three for each of the five cross-sectional member sizes, revealed variations that significantly impacted the strength, ductility, failure modes, and yield plateau but not stiffness. The mean values of the obtained parameters and thicknesses are presented in **Table 1**, while the test setup and tensile stress-strain curves of the coupons are depicted in **Fig. 2 and Fig. 3(a~e)**. These findings were employed to determine the material input parameters for the FEM.

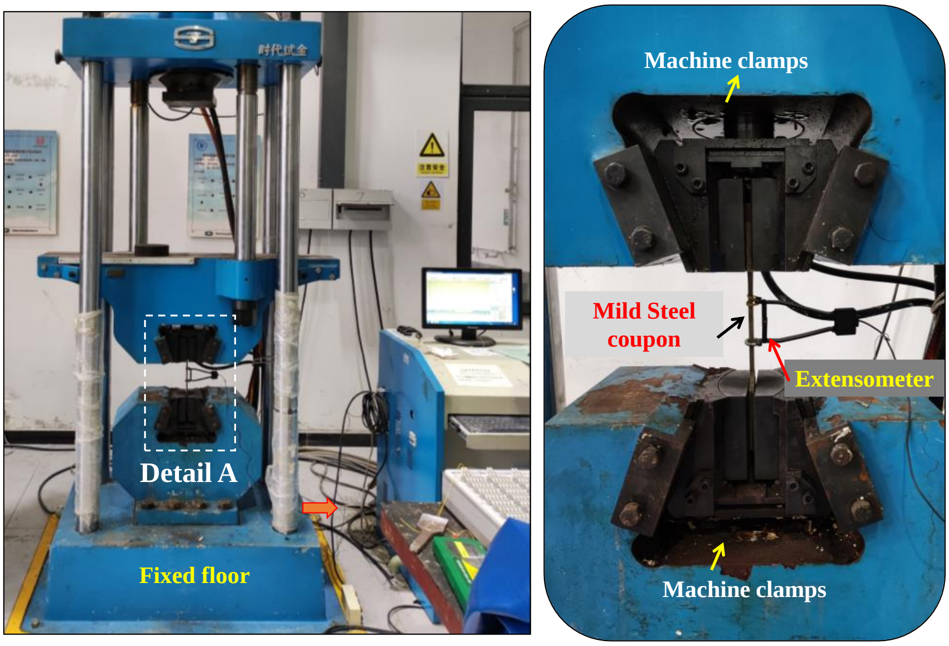

Real-time testing Detail A

Fig. 2 Description of steel coupons and setup for material testing

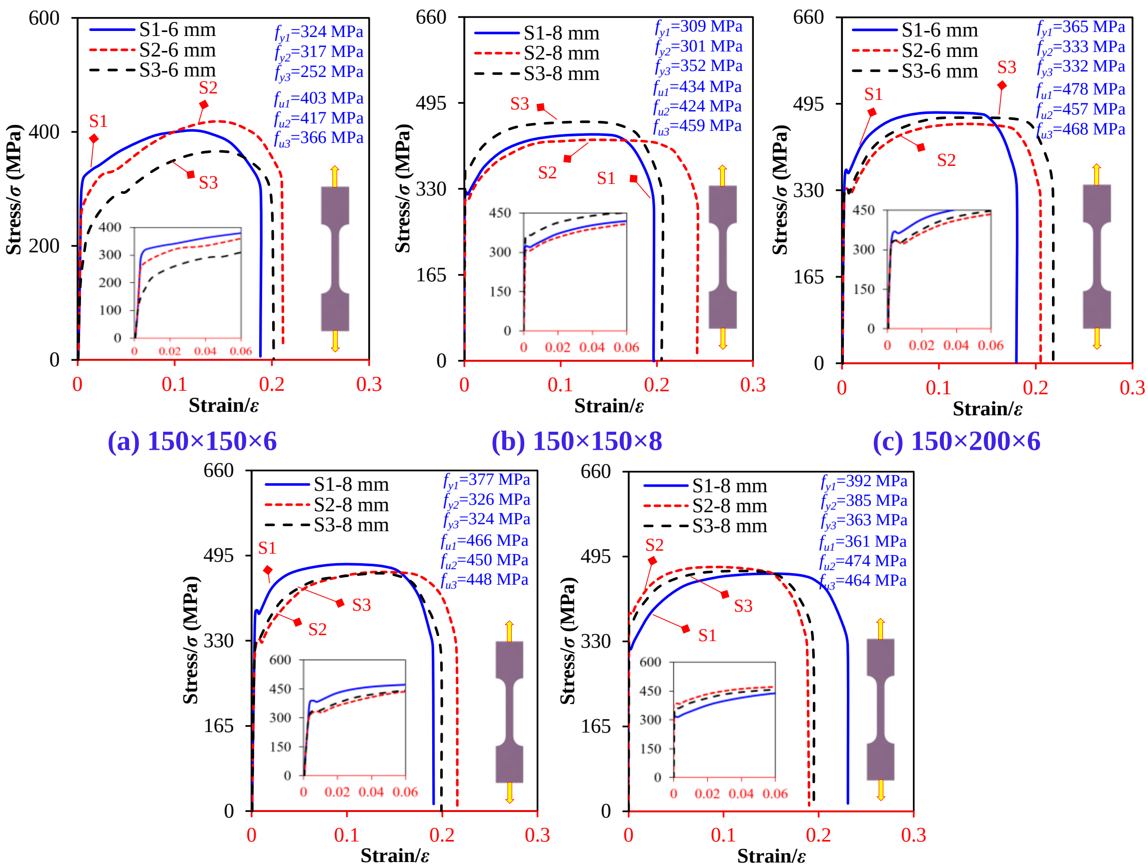

(a) 150×150×6 **(b) 150×150×8** **(c) 150×200×6**

(d) 150×200×8 **(e) 200×200×8**

Fig. 3 Tensile testing results of steel coupons

Table 1 Material properties, details, and findings of compression tests and FEMs on rotary-connected SCSMIFs

Item	D_{FB} (mm)	B_{FB} (mm)	t_{FB} (mm)	L_{FB} (m)	D_{CB} (mm)	B_{CB} (mm)	t_{CB} (mm)	L_{CB} (m)	$P_{u,Test}$ (kN)	$K_{e,Test}$ (kN/mm)	$\Delta_{u,Test}$ (mm)	DI_{Test} (Ratio)
RDD-1	150	200	8	1.2	150	150	6	1.2	3793	828	11.1	1.8
RDD-2	150	200	8	1.2	150	150	8	1.2	3646	778	7.2	1.5

Item	$P_{u,Test}$ (kN)	$P_{u,FE}$ (kN)	$\frac{P_{u,Test}}{P_{u,FE}}$	$K_{e,Test}$ (kN/mm)	$K_{e,FE}$ (kN/mm)	$\frac{K_{e,Test}}{K_{e,Test}}$	$\Delta_{u,Test}$ (mm)	$\Delta_{u,FE}$ (mm)	$\frac{\Delta_{u,Test}}{\Delta_{u,FE}}$	DI_{Test} (Ratio)	DI_{FE} (Ratio)	$\frac{DI_{Test}}{DI_{FE}}$
RDD-1	3793	3827	0.99	828	832	1.00	11.1	9.3	1.19	2.0	2.6	0.69
RDD-2	3646	3686	0.99	778	827	0.94	7.2	4.7	1.54	2.0	1.3	1.16
Mean			0.99			0.97			1.37			0.93
Cov			0			0.03			0.13			0.25

Item	Length (mm)	Width (mm)	Thickness (mm)	f_y (MPa)	f_u (MPa)	δ (%)	E_s (GPa)
Beam-1	150	150	6(5.37)	298	395	22.2	201
Beam-2	150	150	8(7.33)	321	439	23.6	209
Beam-3	150	200	6(5.54)	344	468	24.9	208
Beam-4	150	200	8(7.30)	342	455	23.5	210
Column	200	200	8(7.34)	380	434	22.7	206
Corner fittings[1]	-	-	16(15.80)	351	518	23.0	198
IMC (ii, iii)[1]	-	-	-	360	580	34.0	206
IMC (i, iv)[1]	-	-	-	360	610	16.0	206

D_{FB}, B_{FB}, t_{FB}, L_{FB}; D_{CB}, B_{CB}, t_{CB}, L_{CB}; $P_{u,\,Test}$ ($P_{u,\,FE}$), $K_{e,\,Test}$ ($K_{e,\,FE}$), $\Delta_{u,\,Test}$ ($\Delta_{u,\,FE}$), DI_{Test} (DI_{FE}); and f_y, f_u, δ, E_s represent the floor and ceiling beam's width, depth, thickness, length; ultimate compressive resistance, initial stiffness, ultimate shortening, post-ultimate ductility index via test (FEM); material yield strength, ultimate strength, percentage elongation, elastic modulus. Note:[1] Material properties obtained according to the authors' previous Ref. [2] study. The thickness values in the bracket represent the average measured thickness of members.

Table 2 Rotary-connected SCSMIFs' buckling load comparison using tests-validated FEMs, parametric, and theoretical models

Specimen (#)	P_{cr}/FE (kN)	P_{cr}/PD (kN)	P_{cr}/SR (kN)	$\frac{P_{cr}/PD}{P_{cr}/FE}$	$\frac{P_{cr}/SR}{P_{cr}/FE}$
RDD-1	1403	939	1248	0.67	0.89
RDD-2	1367	1019	1337	0.75	0.98
Mean				0.71	0.93
Cov				0.05	0.05
FEM (#)	P_{cr}/FE (kN)	P_{cr}/PD (kN)	P_{cr}/SR (kN)	$\frac{P_{cr}/PD}{P_{cr}/FE}$	$\frac{P_{cr}/SR}{P_{cr}/FE}$
DR-1	1369	784	1210	0.57	0.88
DR-2	1369	850	1303	0.62	0.95
DR-3	1527	1155	1496	0.76	0.98
DR-4	1532	1228	1588	0.80	1.04
DR-5	1673	1272	1660	0.76	0.99
DR-6	1676	1343	1665	0.80	0.99
DR-7	1605	1228	1579	0.77	0.98
DR-8	1116	432	932	0.39	0.84
DR-9	1856	1565	1810	0.84	0.98
DR-10	1299	727	1201	0.56	0.92
DR-11	1768	1652	1862	0.93	1.05
DR-12	1316	840	1294	0.64	0.98
DR-14	851	275	350	0.32	0.41
DR-26	1429	862	1210	0.60	0.85
DR-28	1839	1092	1753	0.59	0.95
DR-40	1427	952	1405	0.67	0.98
DR-42	1746	1111	1805	0.64	1.03

DR-44	1829	1182	2017	0.65	1.10
DR-47	1415	862	1064	0.61	0.75
DR-48	1386	862	1064	0.62	0.77
DR-49	1379	1019	1337	0.74	0.97
DR-50	1347	1019	1337	0.76	0.99
DR-51	1331	1092	1478	0.82	1.11
DR-52	1342	1092	1478	0.81	1.10
DR-55	2086	1019	1337	0.49	0.64
DR-56	2078	1019	1337	0.49	0.64
DR-78	1457	1019	1337	0.70	0.92
DR-79	1348	1019	1337	0.76	0.99
DR-80	1370	1019	1337	0.74	0.98
DR-81	1342	1019	1337	0.76	1.00
DR-82	1344	1019	1337	0.76	0.99
DR-83	1129	1019	1337	0.90	1.18
DR-84	1368	1019	1337	0.74	0.98
DR-85	1375	1019	1337	0.74	0.97
DR-86	1423	1019	1337	0.72	0.94
DR-87	1087	1019	1337	0.94	1.23
Mean				0.69	0.95
Cov				0.20	0.16

P_{cr}/FE , P_{cr}/PD , and P_{cr}/SR define the buckling load of sub-assembled rotary-connected SCSMIFs via FEMs and theoretically-obtained pinned and semi-rigid IMCs models.

2.4 Test setup

Rotary-connected SCSMIF specimens were mounted on the compressive testing setup, as shown in **Fig. 4(a,b)**. Before mounting the specimens on the setup, the left, right, upper, and lower frame skeletons were joined on the ground using rotary-type IMCs following Refs. [2,8–10,40,89]. A vertical hydraulic jack applied a compressive force to the upper columns of specimens. Column roller supports were installed above the jack to allow lateral movement of the specimen while maintaining the compressive load, even during specimen shortening and lateral deflection. The jack base was fixed to a load sensor using a plate and threaded bolts to record the reaction forces. The load sensor was attached at both the top and bottom ends by a jack and double-column knife-edge support using welded plates and threaded bolts. To ensure that the load was transferred promptly to both adjacent upper columns while allowing for rotation, a double-column knife-edge support was welded to the bottom end of the plate, keeping the support flat. The double-column knife-edge support facilitated in-plane rotation, while out-of-plane rotation was restricted. A pin cell supported the lower columns base, which provided double-column hinged support that prevented specimens from translating in-plane and out-of-plane directions while allowing in-plane rotation. Roller supports were installed on the ends of beams of both the right and left modules to restrict vertical translation while allowing for in-plane translation and rotation. In Ref. [88], a similar testing method was suggested as a standard for simulating the behavior of SCSMIF under sway-frame conditions, as detailed in [2,8,10,36,46,48,89,91,93]. A laser level ensured the specimen and load setup were aligned correctly. Once the alignment was confirmed, the jack was pressed slightly to ensure they remained vertical. Measuring devices were then installed before the formal testing began.

According to GB/T50344-2019 [94], the loading process was divided into preloading and formal loading, with unloading occurring in both stages. The measuring devices' precision was validated using a preload equivalent to $0.2P_u$ (SCSMIF's ultimate compressive resistance). The specimens were kept at the preload level for two minutes before being wholly unloaded for another two minutes. In order to account for structures with unpredictable yield displacements, a loading approach that combined force and displacement control was employed [95]. Following force loading until yielding, a displacement loading rate of 0.05 mm/min was adopted until the load dropped to 85% of P_u [96]. Once the non-linear segment of the load-shortening curves began, displacement loading was accomplished using reaction forces captured through the load sensor and shortening measured by the vertical LVDT (V5 in **Fig. 1(a)**).

Strain gauges were utilized to evaluate deformation and force transfer mechanisms [97]. As shown in **Fig. 5(a,b)**, several strain gauges were installed on the upper columns, lower columns, floor beams, ceiling beams, and upper and lower corner fittings to assess local elastic or plastic buckling that occurred either before or after material yield [98]. Due to the susceptibility of columns to local buckling, strain gauges were vertically positioned along their height and on the corner fittings. Furthermore, it was anticipated that columns near the IMCs or the ends would be subjected to higher stresses and ultimately fail. As a result, strain gauges were mounted in various positions on the upper columns, including at the ends and midpoints. Similarly, strain gauges were placed on the lower columns where higher stresses were expected, mainly near the IMCs and ITCs zones up to mid-height. No strain gauges were attached to the mid-to-bottom section of the lower columns, as stresses were less apparent in those regions. As the beams were allowed to rotate and the stress levels near the ITCs and IMCs were high, strain gauges were affixed to a distance of up to 200 mm from these locations. Since the limited space available for work due to the small gap between the floor beam and ceiling beam and the adjacent upper column and lower column, no strain gauges were attached in those areas. A total of 73 strain gauges were utilized in RDD-1, while RDD-2 had 66.

Figure 1(a) shows fourteen horizontal LVDTs placed vertically on adjacent modular units' right and left sides, including lower columns, upper columns, floor beams, and ceiling beams (H1-H14), to measure deflection, translation, sway, or buckling. A vertical LVDT (V5) was also mounted on a double-column jack-fixed knife-edge support to evaluate end-shortening. Four other LVDTs (V1-V4) near ITCs and IMCs measured the vertical deflection of ceiling and floor beams. These deflection, end-shortening, strain, and load measurements were recorded using a data recorder.

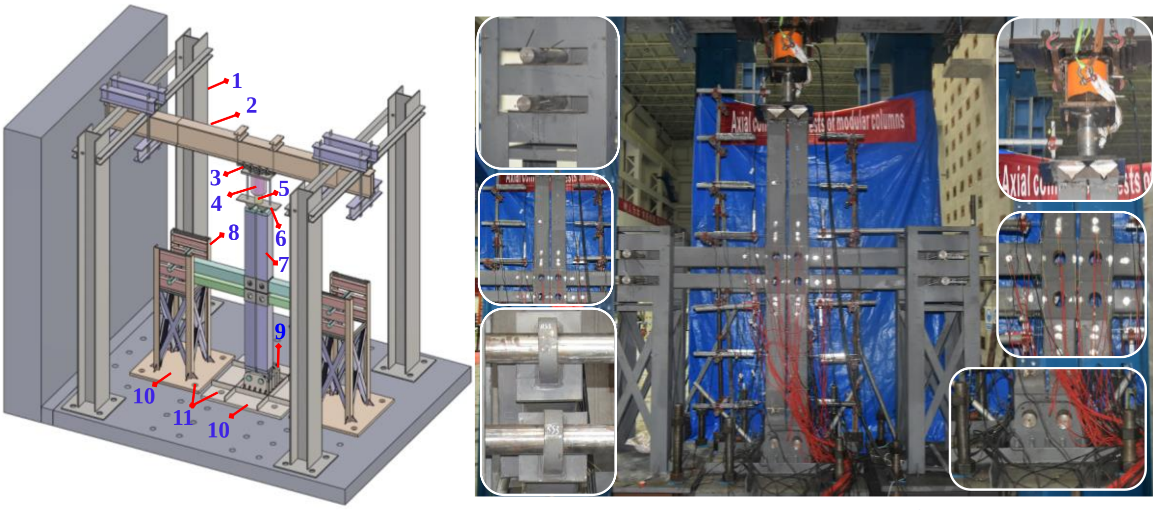

(a) Test setup schematic diagram **(b)** Test setup and specimen before the test

Fig. 4 Generalized compression tests setup on sub-assembled rotary-connected SCSMIFs. (1-Reaction frame; 2-Reaction beam; 3-Column roller support; 4; Vertical hydraulic jack; 5-Load sensor; 6-Double-column knife-edge support; 7; SCSMIF specimen with rotary-type IMCs; 8-Beams roller supports; 9- Double-column hinged support; 10-Pedestal; 11-Anchor bolt holes)

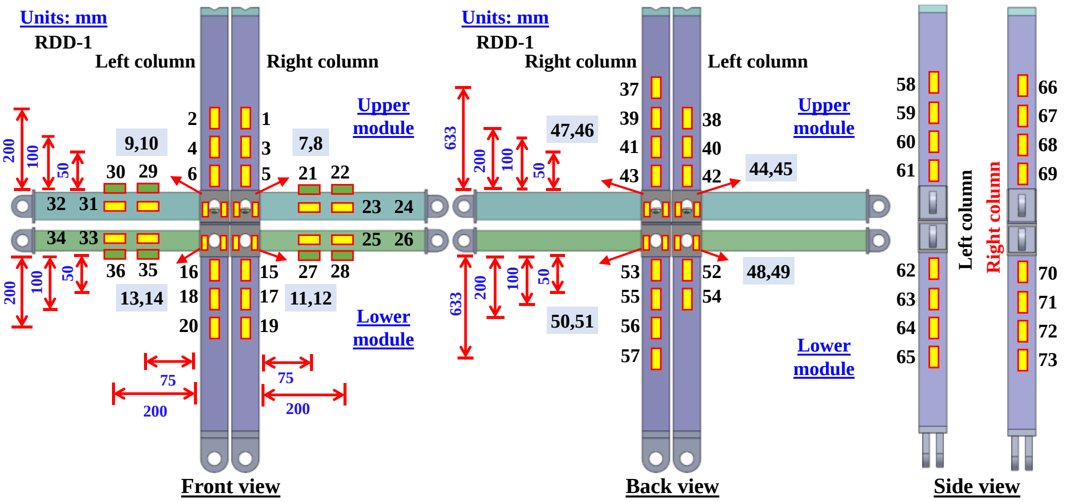

(a) RDD-1 strain gauges

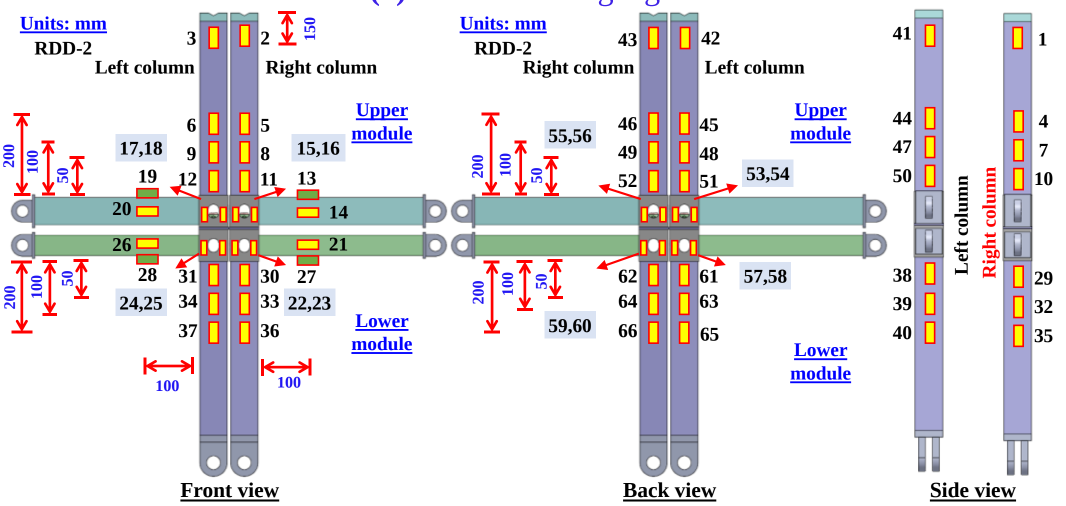

(b) RDD-2 strain gauges

Fig. 5 Specific strain gauge locations on rotary-connected SCSMIFs

3 Experiment outcomes

3.1 Failure modes

As depicted in **Fig. 6(a,b)**, the relative rigidity of the floor beams, ceiling beams, upper columns, and lower columns substantially affected the in-plane translations of RDD-1 and RDD-2. The SCSMIF in RDD-2 was more flexible than in RDD-1, resulting in increased lateral instability. Non-rigid constraints enabled the formation of gaps, rotations, and translations of the upper and lower frame skeletons around the rotary-type IMCs, which pinned or rigid assumptions cannot simulate. Upon reaching their compression capacity, the SCSMIFs experienced simultaneous local buckling of adjacent upper columns, forming S-shaped inward and outward patterns with similar placements on adjacent columns. Once buckling occurred, the SCSMIFs could not support additional load, necessitating a loading halt for safety purposes. Strain values indicated that in RDD-1, local buckling happened at a distance of 100-200 mm on all top faces of upper columns due to reduced sway, whereas in RDD-2, it occurred at the base of the upper columns approximately 100-200 mm from the corner fittings due to significant bending. Columns of RDD-1 bulged outward on their inner sides, while columns of RDD-2 bulged inward, resulting in a double S-shaped local buckling and preventing collisions on the inner sides.

Comparisons of material yield in **Fig. 8(a~c)** revealed that the upper columns experienced local elastic buckling in regions aligned with or opposite the bending direction. In other areas, local plastic buckling was observed. The beams and corner fittings did not buckle or yield before reaching the SCSMIF's capacity, but several upper column regions yielded, indicating that the upper columns bore the primary load. The absence of out-of-plane translation and rotation adjacent to the bending sides meant that the compressive behavior of SCSMIF was primarily controlled in the in-plane direction. Although the local buckling location varied between the two specimens, IMCs could transmit force to adjacent members without any localized failure, suggesting that rotary-connected SCSMIFs could ensure the safety and integrity of MSBs under compressive loads.

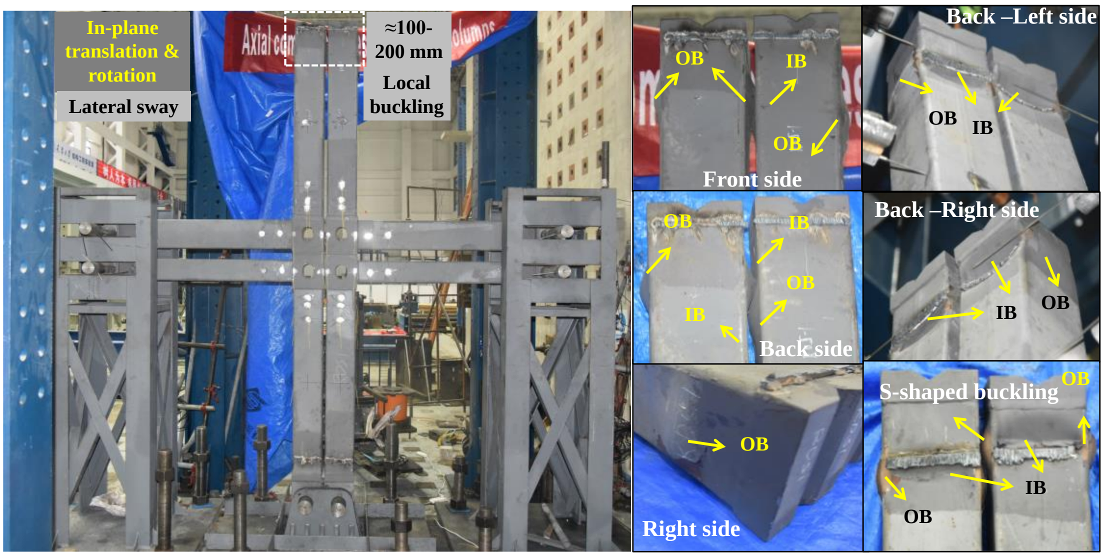

Overall deformed front view Failure modes detailed views

(a) RDD-1

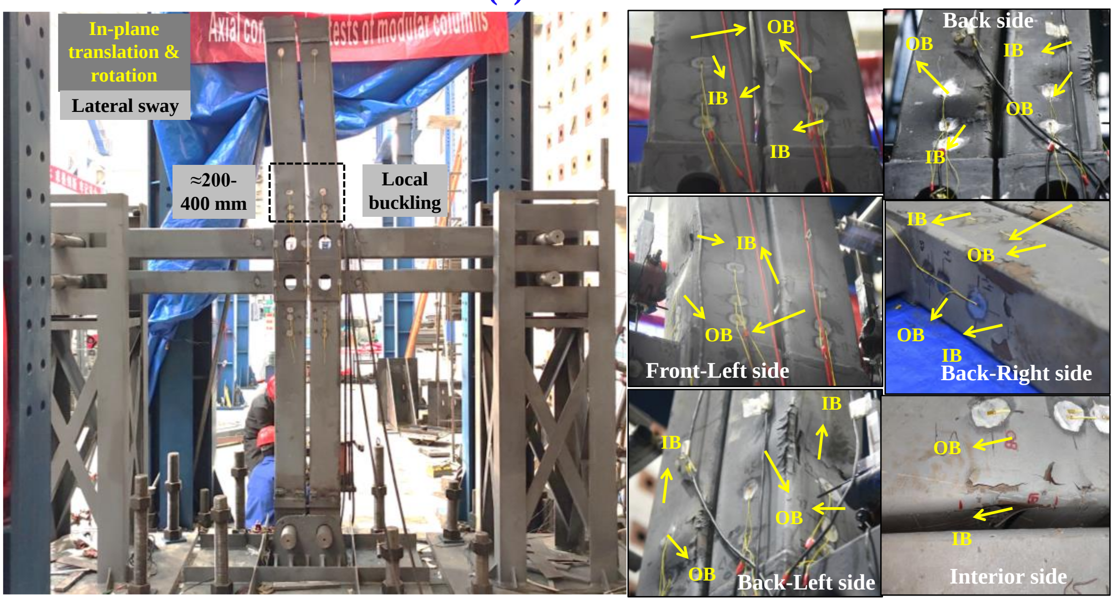

Overall deformed front view Failure modes detailed views

(b) RDD-2

Fig. 6 Failure modes of rotary-connected SCSMIFs (IB/OB, inward/outward buckling)

3.2 Load-shortening curves

Figures 7(a,b) and **7(e)** illustrate load-shortening curves and the general behavior of RDD-1 and RDD-2 rotary-connected SCSMIFs. These curves reveal the elastic (I), inelastic (II), and recession (III) stages of the SCSMIFs, which can be used to calculate their ultimate compressive resistance (P_u), ultimate shortening (Δ_u), initial stiffness (K_e), and ductility index (DI) [99,100]. In stage I, the load increases proportionally with shortening until the yield strength (P_y) is attained. After reaching P_y, the capacity increases as the stiffness of curves decreases because buckling and bending stresses are exceeded at various upper column locations, such as the top in the RDD-1 and the bottom in the RDD-2. The curves take on a parabolic shape throughout stage II, beginning from P_y and continuing until P_u. Meanwhile, a symmetrical inward and outward local buckling pattern emerges simultaneously on both adjacent upper columns. When comparing RDD-1 and RDD-2, it was found that the P_u of RDD-2 was 3.9% lower, and K_e decreased by 6%. This suggests that RDD-2 was less rigid, leading to more significant sway, bending stresses, and secondary moment effect, which decreased SCSMIF strength and stiffness. Strain values confirmed that local elastic buckling mainly resulted in noticeable SCSMIF compressive behavior reduction and premature instability in the RDD-2. As shown by Δ_u, RDD-2 demonstrates 35% less pre-ultimate ductility than RDD-1. This results from the SCSMIF's reduced flexibility, which increases buckling strain and ductility. In contrast, RDD-1 can better resist compressive forces, experience less sway and deformation, and minimize bending and shear stresses in its members, attaining higher strength, stiffness, and ductility levels. Stage III is characterized by decreased capacity, an abrupt increase in deflection, and severe local buckling; thus, the DI of SCSMIFs are compared. In this post-ultimate stage, the recession follows the ultimate stage and is marked by an abrupt decline in capacity that may persist until a larger end-shortening [101–107]. RDD-1 had a 48% higher ductility index and a superior recession stage than RDD-2, indicating it can withstand more significant deformations while preserving its structural integrity and preventing stress transmission to its components.

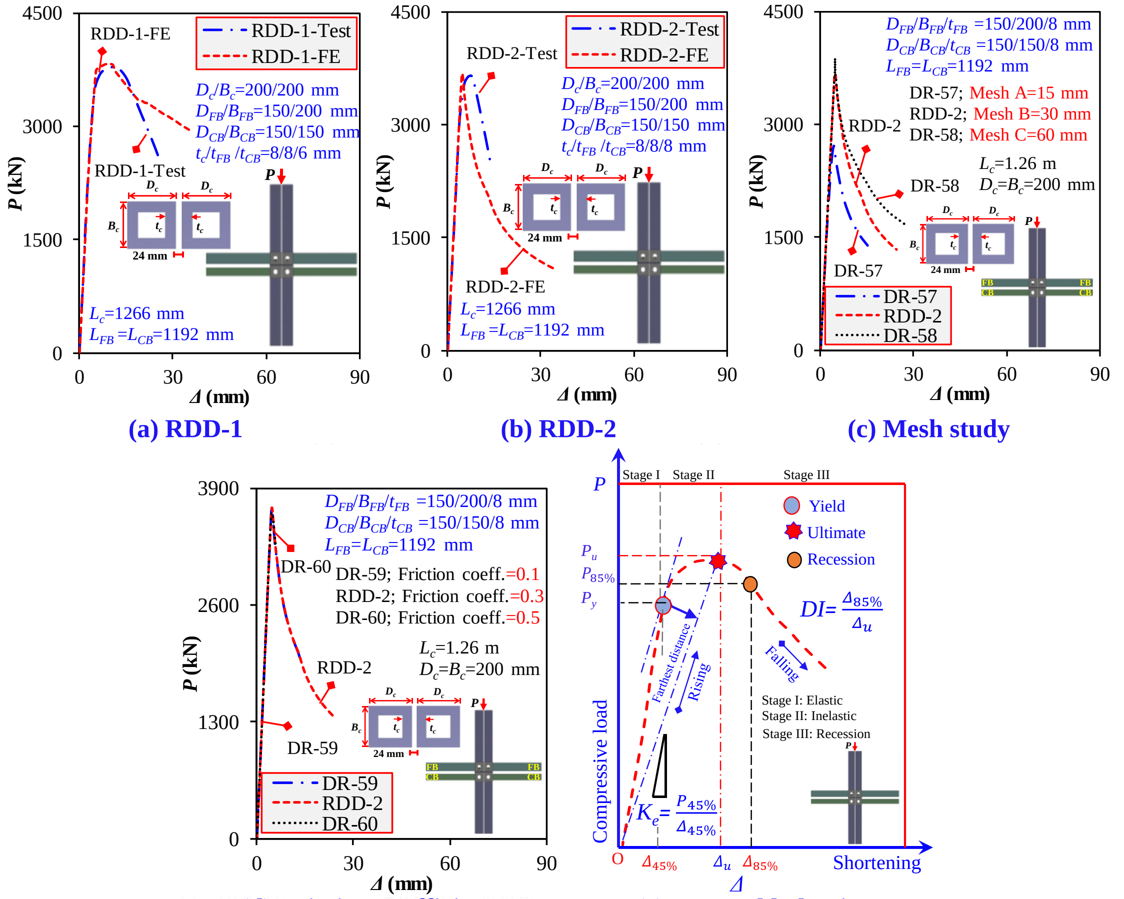

(a) RDD-1 **(b) RDD-2** **(c) Mesh study**

(d) Friction coefficient **(e) General behavior**

Fig. 7 Load-shortening curves of rotary-connected SCSMIFs

3.3 Load-strain curves

Figures 8(a~c) and **9(a~m)** depict load-strain curves for SCSMIFs' columns and strain magnitudes on upper and lower corner fittings, upper columns, lower columns, floor beams, and ceiling beams, highlighting the strain amount, yield strain, and local buckling sites. The curves' linear, non-linear, and recession sections identify test failure types and local buckling locations, whether apparent or not. As the load increases, the stresses increase until local buckling is indicated by the inversion, overturning, or rapid decline of strain curves and exceptionally high strain values. Curves that reverse before or around the yield strain show stresses below the material's yield strength, resulting in elastic buckling. In contrast, plastic buckling occurs when stresses exceed the yield strain. Additionally, the appearance of overturning curves during the recession phase following the yield strain indicates the emergence of severe local plastic buckling. The failure modes, significant strain values, and curves indicate the presence of symmetrical S-shaped local inward and outward buckling in the lower regions of both adjacent upper columns in RDD-2 and top areas of RDD-1, with these buckling patterns occurring circumferentially on all column faces at 100-200 mm. Despite evident local buckling in upper columns, no buckling or yielding was detected in many areas of lower columns. Furthermore, most other members, such as floor beams, ceiling beams, and lower and upper corner fittings, did not yield because the maximum strain values recorded in tests were generally low. This indicates no adverse localized deformation in the rotary-type IMCs and SCSMIFs' other members, except for the columns, which were the primary load-carrying members.

Since no strain gauge was on the RDD-1 local buckling location, more extensive strain measurements or curve overturning were observed at top locations 2 and 4 in RDD-1. Likewise, bottom locations 4, 5, 6, 7, 10, 11, 44, 45, and 49 in RDD-2 demonstrated the existence of local buckling on each face of the upper columns, displaying both local elastic and plastic buckling. In RDD-2, upper column portions experiencing bending stresses in or opposite directions of the beams exhibited elastic buckling, while adjacent upper column sides not exposed to bending underwent plastic buckling. For example, locations 4, 7, and 10 in RDD-2 displayed local elastic buckling, indicating that bending and the secondary moment effect prevented upper columns and other members from completely yielding.

3.4 Load-deflection curves

The load-deflection curves in **Fig. 10(a~h)** show linear, non-linear, and recession phases followed by a curve drop. The length of the curves indicates in-plane translations as measured by the deflection amount. The varying stiffness reduction of each curve reveals that members respond differentially to the magnitude of the *P*-delta effect.

However, the relative members' stiffness effect caused SCSMIF to be more flexible in RDD-2. This resulted in higher lateral deflection of members than in RDD-1. As the load increases, the deflection also rises, stabilizing when the ultimate capacity is reached, followed by a pause in load but deflection increments. The orderly increase in deflection from lower to upper columns on the right and left frame skeletons indicates the presence of SCSMIF sway and local buckling. The maximum deflection at the top of the upper columns in RDD-2 suggests the instability of SCSMIFs due to local and global failure. Non-identical deflections of floor and ceiling beam in vertical and lateral directions and their difference imply a degree of relative rotation between the upper and lower frame skeleton at rotary-type IMCs. This cannot be simulated as rigid or pinned [32].

The deflection curve validates the test failure modes. The apparent deflection difference between the top and bottom ends of the upper columns, as illustrated by H8/H9 and H6/H11, indicates that local buckling began near H6/H11, followed by an increase in lateral deflection at the top H8/H9 in RDD-2. In addition, the deflection curves of the right and left frame skeletons exhibit an apparent resemblance in RDD-1 and RDD-2, suggesting that both structures behaved symmetrically, resulting in identical local buckling at corresponding locations on adjacent upper columns. These findings indicate that the rotary-type IMCs transmitted forces and that the left frame skeleton had no detrimental effect on the deformation behavior of the right frame, consistent with existing literature [49].

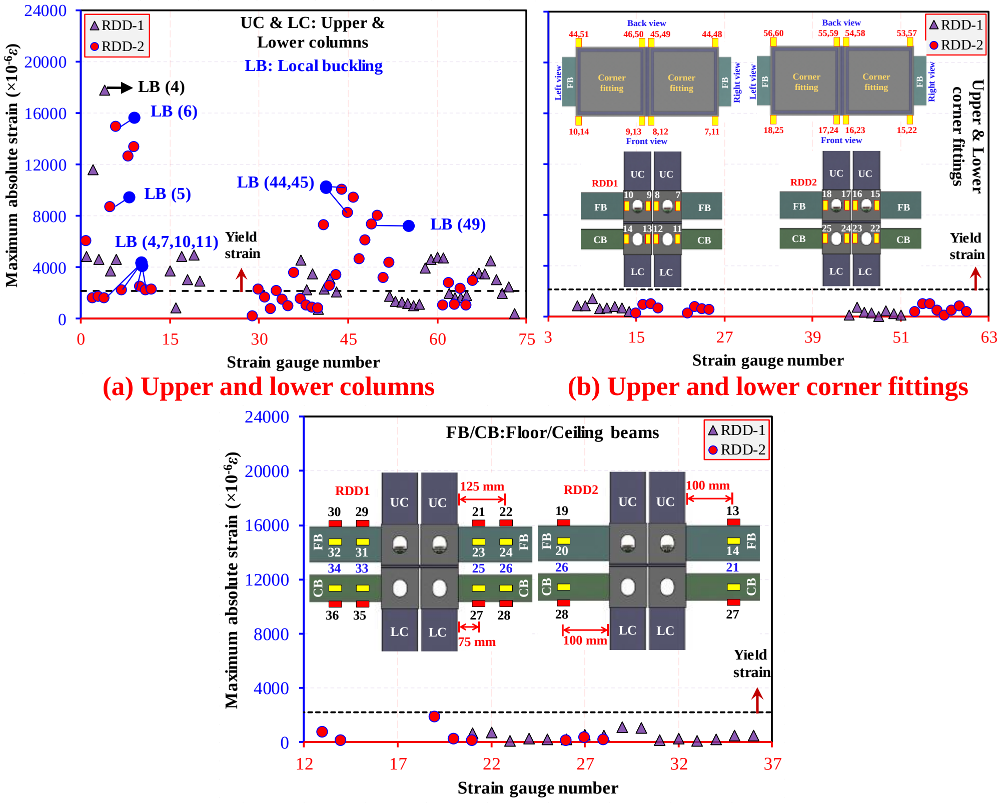

(a) Upper and lower columns
(b) Upper and lower corner fittings
(c) Floor and ceiling beams

Fig. 8 Part-wise maximum absolute strain distribution of SCSMIFs

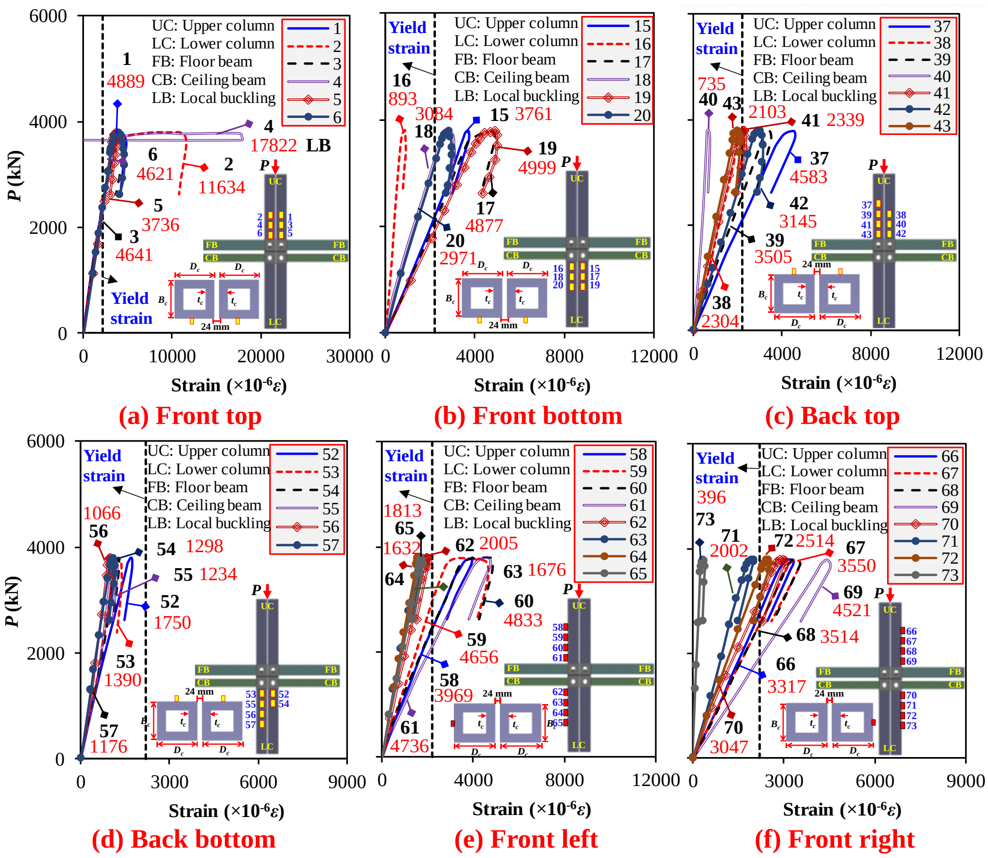

(a) Front top
(b) Front bottom
(c) Back top
(d) Back bottom
(e) Front left
(f) Front right

RDD-1 columns strain curves

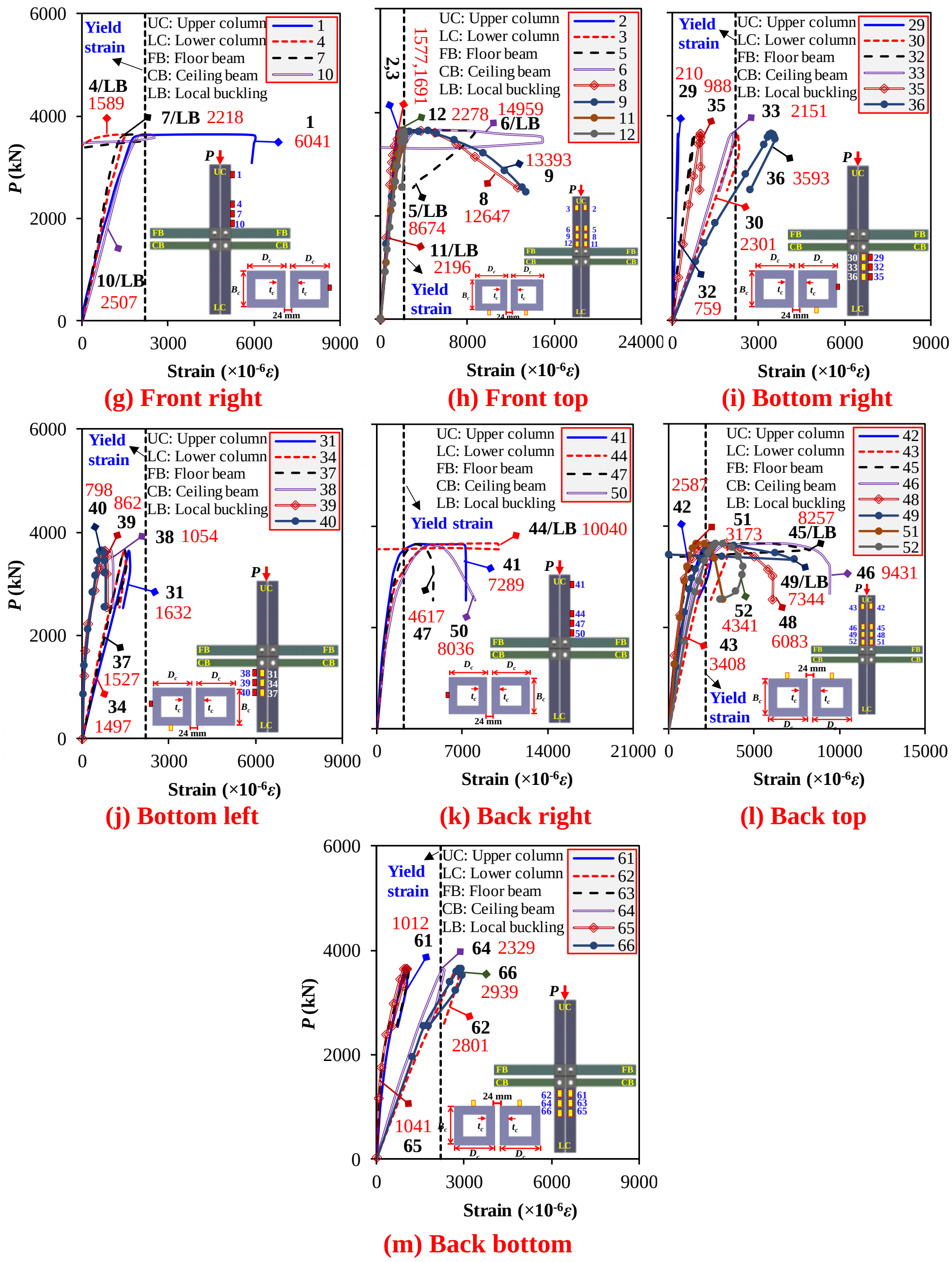

RDD-2 columns strain curves

Fig. 9 Load-strain curves at columns of SCSMIFs

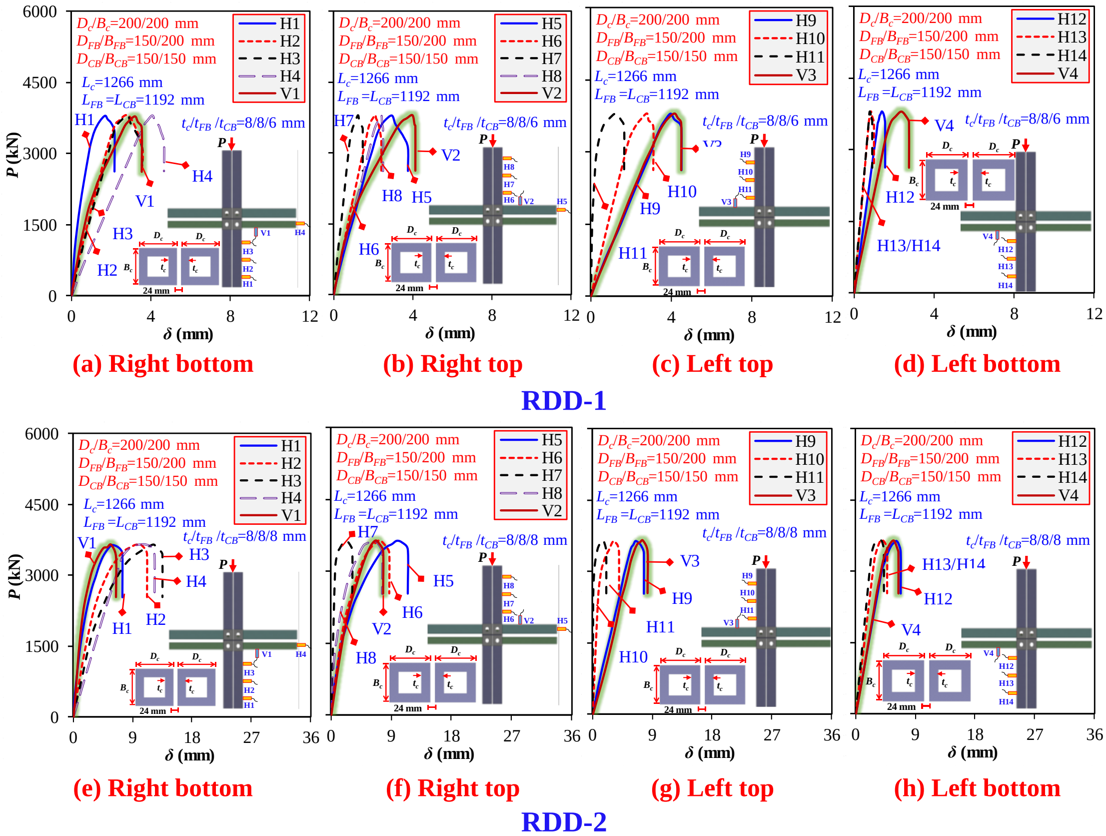

Fig. 10 Load-deflection curves at various parts of SCSMIFs

4 Finite element analysis of rotary-connected SCSMIFs

Although the tests provided valuable information on the behavior of the SCSMIFs, they did not fully assess their overall instability or the effect of varying parameters on their elastoplastic compressive behavior. A 3D non-linear FEM was developed to address these limitations using data extracted from load-shortening curves and failure modes observed during testing.

4.1 Development of finite element model

ABAQUS [108] was utilized for finite element modeling and analysis. Elastic buckling analysis was performed with the ABAQUS/Linear perturbation buckle-type solver and the subspace iteration approach to determine buckling loads and modes. Non-linear analysis was conducted with the ABAQUS/static Riks-type solver to investigate load-shortening behavior and failure mechanisms. The bilinear kinematic hardening and von

Mises yield criteria were applied to all components, with material properties taken from **Table 1** [32]. A Poisson's ratio was set to 0.3 [89].

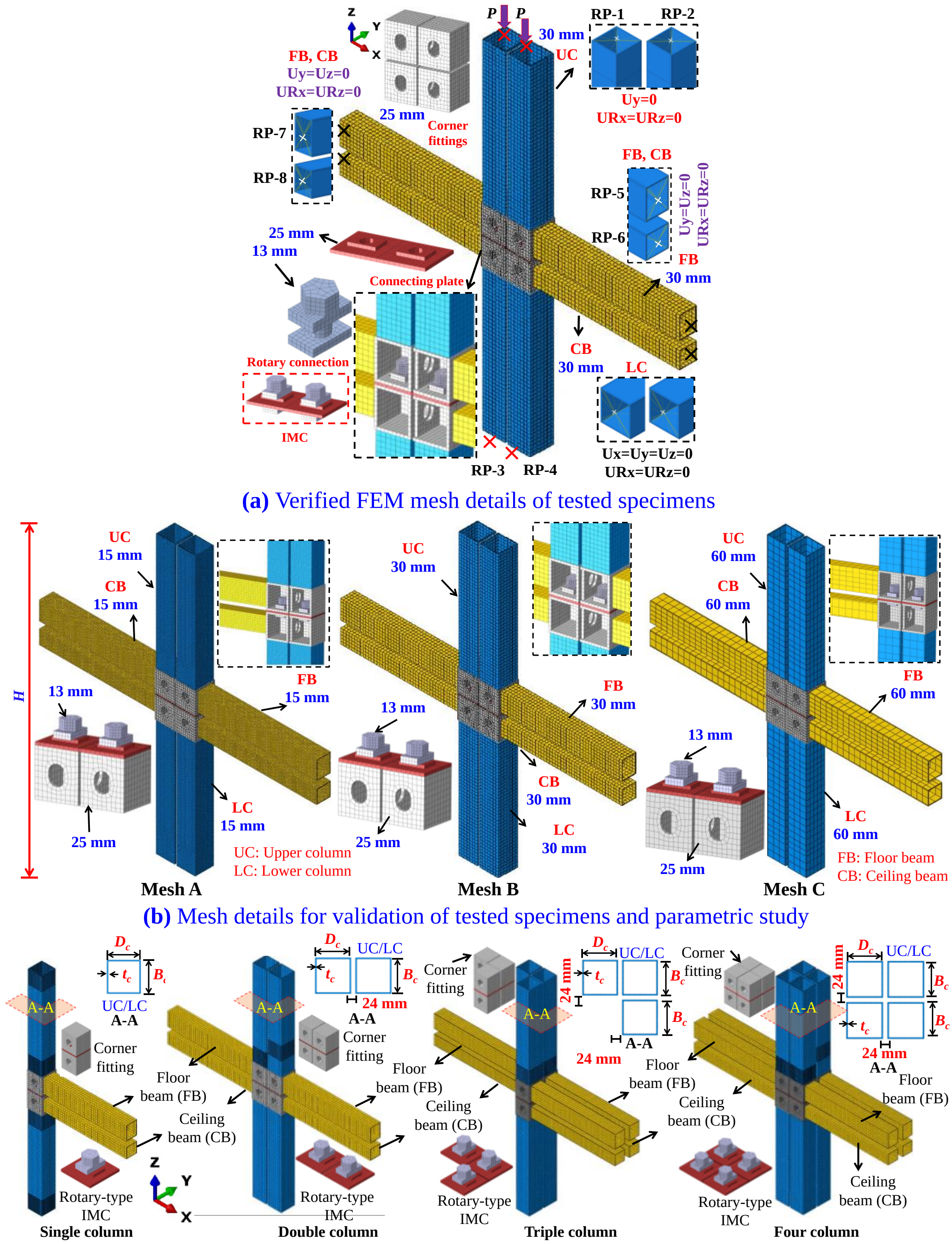

(a) Verified FEM mesh details of tested specimens

(b) Mesh details for validation of tested specimens and parametric study

(c) Varying column number details of FEMs

Fig. 11 Details of experimentally-validated and parametric FEMs of rotary-connected SCSMIFs

4.2 Mesh modeling

Figure 11(a) shows the mesh model for RDD-1 and RDD-2, which includes corner fittings, upper columns, lower columns, floor beams, ceiling beams, and rotary-type IMCs. Different mesh sizes and the specifics of various column numbers are depicted in **Figs. 11(b,c)**. All member dimensions were designed to be comparable to the actual specimens and were modeled as 8-node linear brick, reduced integration with hourglass control elements (C3D8R) [109]. The mesh convergence study performed to assess the element size suitability involved comparing the results from mesh A, B, and C with test P-Δ curves, as displayed in **Figs. 7(a~c)**. To more accurately replicate the observed local buckling and deformation characteristics, the column locations at the upper edges for RDD-1 and the lower area for RDD-2 were densely meshed at 100-200 mm with 5 mm, while other regions and parts uniformly meshed. The same technique was followed in Refs. [8,32] to capture the formation of potential local buckling at members. The corners of columns and beams were partitioned at their thickness to create the structured mesh [31,110–112]. Mesh A and B mimicked local buckling and deformation more precisely than Mesh C, as evidenced by the RDD-2 column bottoms in **Fig. 16(c)**. When the mesh size increased from 15 to 30 and 60 mm, P_u (K_e) increased by up to 36% (4%) and 43% (8%), while Δ_u increased by 8%, and DI was reduced to 3%. Moreover, the mesh refinement technique used in Refs. [8,32] capture the formation of prospective local buckling at members did not affect the location of the failure mode where initial imperfections play a crucial role in causing buckling failure. Nevertheless, mesh refinement made the deformation patterns of previously identified test failure locations more apparent. The impact of mesh sizes on compressive behavior was substantial, revealing that Type B mesh yielded the most precise results, emphasizing compression tests on rotary-connected SCSMIFs to determine the appropriate mesh density.

4.3 Loading and boundaries

The columns and beams were subjected to loading and boundary conditions by defining reference points (RP-1~RP-8) on cross-sections and applying surface-based coupling constraints to limit translations and rotations at the coupling nodes. The lower columns were restricted in all directions, while the upper columns, floor beams, and ceiling beams were permitted in-plane translation, but beam vertical translations were restrained. The beams and columns were only allowed in-plane rotation, as their out-of-plane rotation was restricted. The upper columns were subjected to an equal compression force as a displacement-controlled loading at their respective reference points to achieve shortening, and loading was determined by summing up both columns. The ITCs were achieved by welding columns and beams to corner fittings using "tie constraint" via surface-to-surface contact. The interaction between corner fittings, connecting plate, and rotary-type IMC components were simulated as surface-to-surface contact with "hard contact" as normal and "finite sliding" as tangential behavior, using a friction coefficient of 0.3 displayed in **Fig. 7(d)** [109,113,114]. The specimens used in this study were hot-rolled sections with low bending, welding deformation, and residual stresses. Hence, the effects of bending, welding, and temperature residual stress were not considered in the FEM analysis [115,116].

4.4 Initial imperfections

The rotary-connected SCSMIFs consisted of upper columns, lower columns, floor beams, ceiling beams, corner fittings, and IMCs, all of which may have imperfections before and after installation that are challenging to measure with conventional techniques [100]. For reliable outcomes, design standards advise imperfections between t_c/500 to t_c/200 and L_c/1000 to L_c/1996 [117]. However, in SCSMIFs, imperfections can be attributed to local and global factors, i.e., column thickness (t_c), frame height (H), and eccentricity (e) [27,71,72,118]. This study selected specific values for height imperfection, thickness imperfection, and load eccentricities, including $H/500$, $H/1000$, $H/1500$, and $H/2000$ for height imperfections; $t_c/1000$, $t_c/100$, $t_c/10$, t_c, and $2t_c$ for thickness imperfection; and 0, $D_c/70$, $D_c/35$, $3D_c/100$, $D_c/14$, $4D_c/14$, $6D_c/14$, and $3.43D_c/7$ for load eccentricities. The buckling modes depicted in **Fig. 14(a~f)** were determined using an Eigenvalue analysis. A non-linear Riks analysis was performed, including imperfections and load eccentricities per test failure mode shown in **Fig. 6(a,b)**, such as in the frame sway direction. In comparing the buckling modes obtained from Eigenvalue analysis to the failure modes in Riks analysis, the lowest buckling mode (Mode 1) was selected for RDD-1 and RDD-2 to incorporate imperfections, taking into account their precision as recommended in Ref. [73]. The critical buckling loads and accompanying mode shapes were then compared with the loads at which failure occurred in the Riks analysis for a reliable description of the structure's behavior. The imperfection amplitude determined in **Fig. 12(a~c)** was used for rotary-connected SCSMIFs and FEMs of parametric studies in **Supplementary Table A1**. The local imperfection of $H/600$ or $0.64t_c$ and global imperfection of e=$3D_c/100$ produced the closest results to the test outcomes of RDD-2. Like RDD-1's test results, the local imperfection of $H/600$ or $0.64t_c$ and global imperfection of e=$7D_c/500$ produced the most comparable outcomes. **Figures 12(a~c)** and **13(a~f)** demonstrate that increasing H or t_c imperfection values had no noticeable impact on P_u (K_e) and Δ_u (DI). The imperfection values, particularly the load eccentricity values, were influential in determining the failure location in the specimens and reorganizing them on top of the upper columns in RDD-1 and the bottom of the upper columns in RDD-2. Since translation or rotation is permitted in SCSMIFs, the eccentricity effect on P-Δ curves, P_u, K_e, Δ_u, DI, and failure modes was substantial, as shown in **Supplementary Figure B1**.

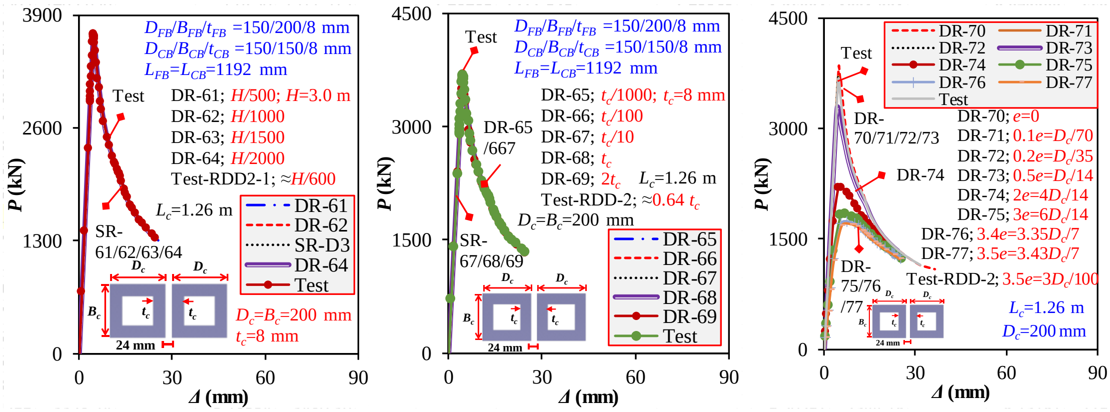

(a) Local imperfection *H* **(b) Local imperfection t_c** **(c) Global imperfection *e***

Fig. 12 Impact of initial imperfections amplitudes on load-shortening curves

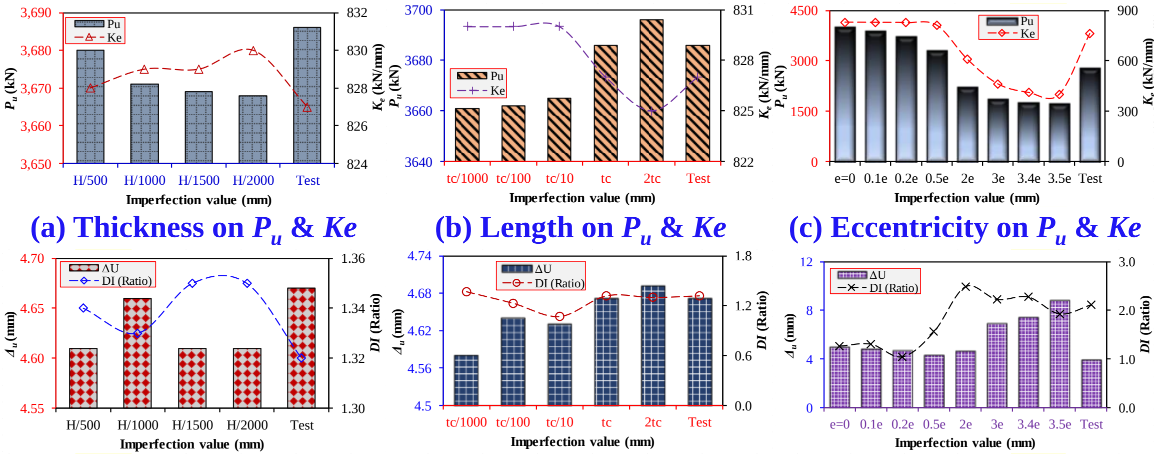

(a) Thickness on P_u & *Ke* **(b) Length on P_u & *Ke*** **(c) Eccentricity on P_u & *Ke***

(d) Thickness on Δ_u & *DI* **(e) Length on Δ_u & *DI*** **(f) Eccentricity on Δ_u & *DI***

Fig. 13 Influence of initial imperfections on compressive behaviors of RDD-2

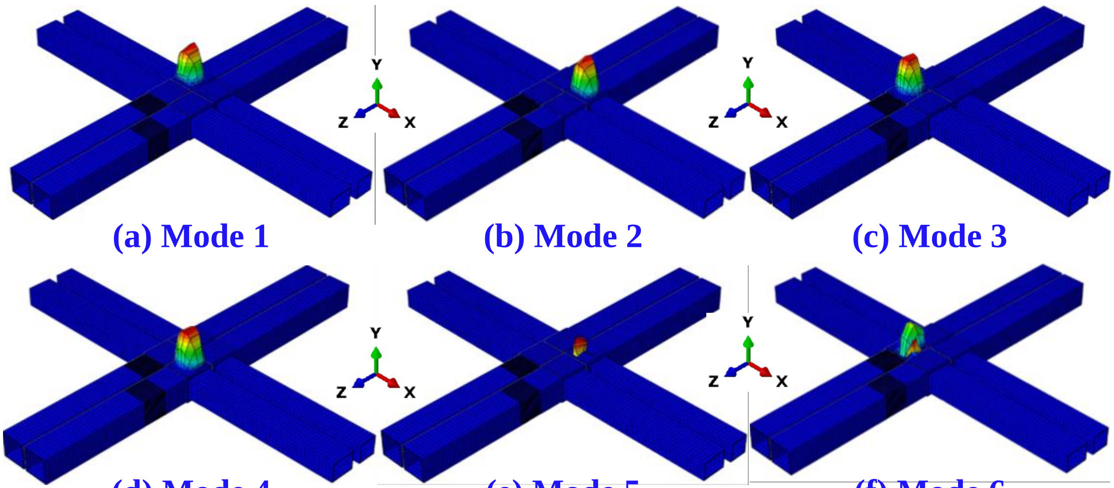

(a) Mode 1 **(b) Mode 2** **(c) Mode 3**

(d) Mode 4 **(e) Mode 5** **(f) Mode 6**

Fig. 14 First six buckling modes of SCSMIFs

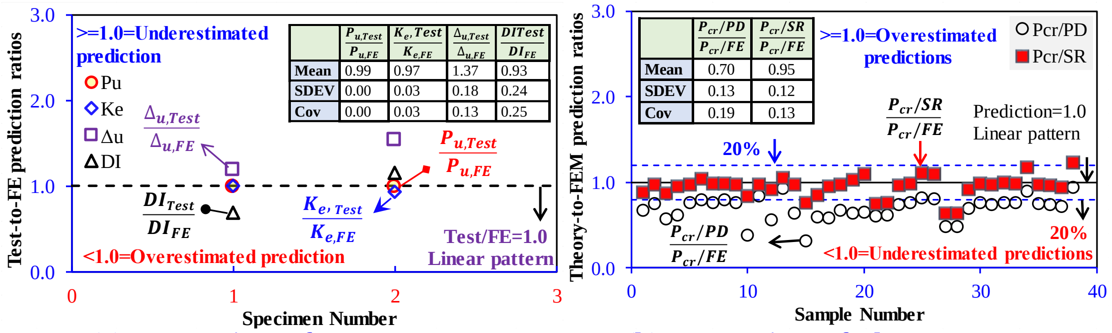

(a) Comparison of Test-to-FEM (b) Comparison of Theory-to-FEM

Fig. 15 Validations of FEMs and theoretical models outcomes

4.5 Validations

Figures 7(a,b) and **15(a)**, as well as **Table 1**, show the average estimates for *P-Δ* curves, P_u, K_e, Δ_u, and *DI* produced by the FEMs for two tests. The results indicate that the FEMs exhibited average modest prediction errors of 1%, 3.2%, and 7.9% for P_u, K_e, and *DI*, respectively. However, there was a significant scattering of 36.6% for Δ_u, mainly due to FEMs simplifications, soft supports, material modeling, and variations in imperfections. The developed FEM can accurately simulate the deformed shapes of SCSMIFs, including S-shaped inward and outward local buckling on all faces at the adjacent upper columns top areas in RDD-1 and lower zones with equal sway in RDD-2, as depicted in **Fig. 16(a,b)**. These validations demonstrate that the proposed FEMs can reliably predict the compressive behavior of rotary-connected SCSMIFs and can be used for further extensive parametric and theoretical investigations.

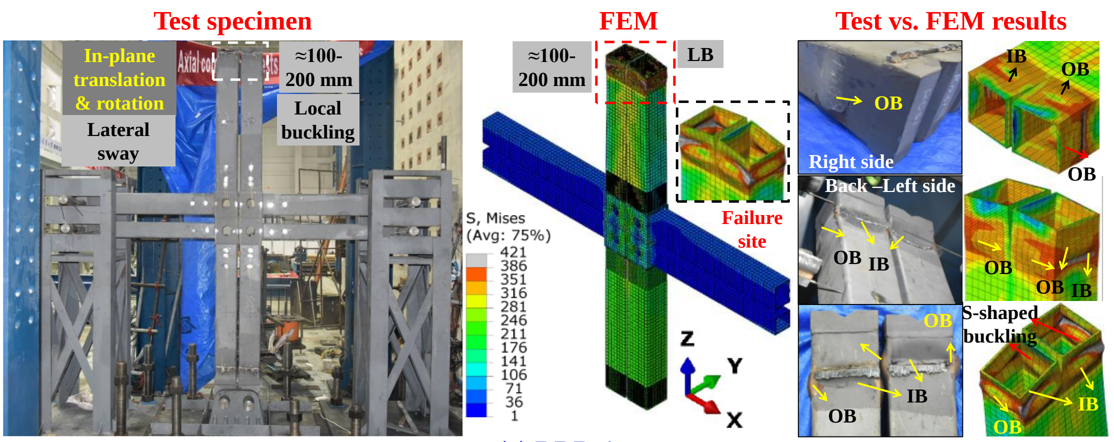

(a) RDD-1

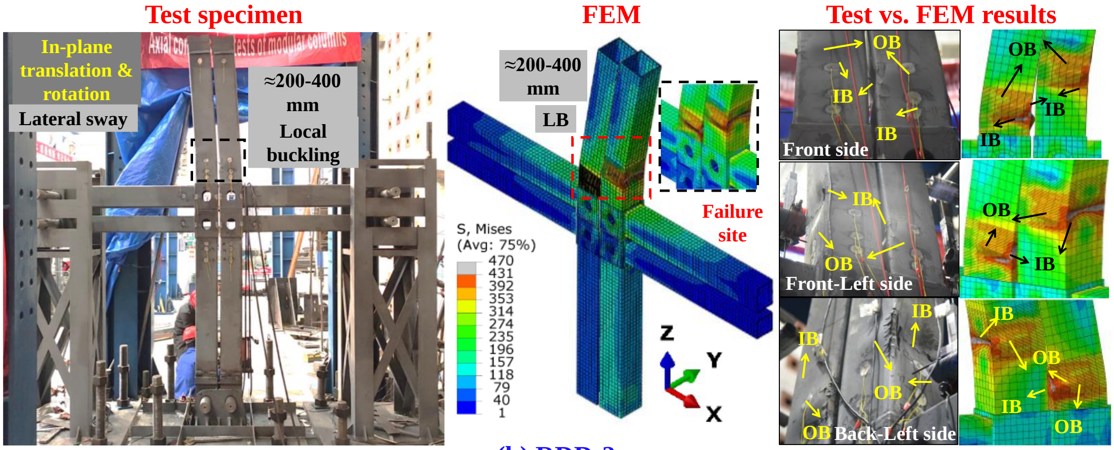

(b) RDD-2

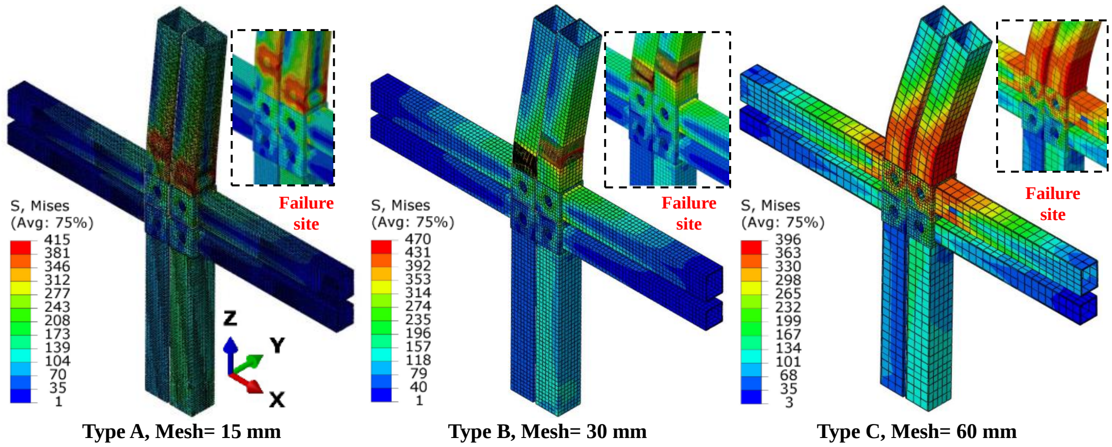

(c) Mesh effect on RDD-2

Fig. 16 Comparison of test and FE-predicted failure modes

5 Parametric analysis

Experimental and numerical validations revealed that RDD-2, with significant sway of the SCSMIFs, possessed lower strength, stiffness, and ductility than RDD-1. Therefore, RDD-2 FEM was used for further parametric investigation. It allows for a more conservative design, better accounting for uncertainties and variations in material properties, fabrication, and installation, ensuring safety in design. The validated FEM produced data for 87 rotary-connected SCSMIFs, maintaining the dimensions of the rotary-type IMCs and corner fittings, 30 mm Type B mesh, local imperfection of $H/600$ or $0.64t_c$, and global imperfection of $e=3D_c/100$. The parametric analysis involved beam and column sizes, lengths, gaps, quantities, and connecting plate thicknesses. The load-shortening behavior of parameters is presented in **Fig. 17(a~i)**. **Supplementary Figures B1(a~l), B2(a~i),** and **B3(a~i)** illustrate the failure modes, P_u (K_e) trends, and

Δ_u (DI) trends observed in all 87 SCSMIFs. Moreover, **Fig. 18(a~f)** classifies typical behaviors observed in parametric studies, which resemble the test results, indicating that local buckling and lateral sway are predominantly linked to observed behaviors. Similarly, **Fig. 19(a~d)** depicts the failure modes of SCSMIFs with varying quantities of columns. **Supplementary Table A1** outlines each parameter's design details and values for P_u, K_e, Δ_u, and DI.

5.1 Beams cross-sections (D_{FB}×B_{FB}×t_{FB}; D_{CB}×B_{CB}×t_{CB})

Figure 17(a) shows how SCSMIF compressive behavior is affected by D_{FB}, D_{CB}, B_{FB}, B_{CB}, t_{FB}, and t_{CB}, measuring 150 and 200 and 6 and 8 mm while retaining other members' dimensions as prototype design. The outcomes reveal that increasing beam cross-sections improves SCSMIF performance by enhancing P_u and Δ_u in the 4~9% and 3~10% range but lowers DI by 1~20%. When beams' width, depth, and thickness are raised, it boosts structural integrity and prevents premature buckling, allowing SCSMIFs to deform more before reaching their capacity (as seen in **Supplementary Figure B1(a)**). However, there may be a compromise with post-ultimate ductility; therefore, synchronizing these factors is essential for maximizing the performance of SCSMIFs.

5.2 Beams lengths (L_{FB}; L_{CB})

Figure 17(b) illustrates increasing beam lengths from 0.6 to 1.2 and 3 m for a given D_{FB}, D_{CB}, B_{FB}, and B_{CB} of 150 and 200 mm and t_{FB} and t_{CB} of 8 mm while keeping other members consistent with prototype design can negatively impact SCSMIFs P_u (K_e) by impairing them up to the range of 2~16% (1~2%). This is attributed to the increased slenderness of longer beams, which reduces their bending resistance and can lead to premature buckling, hindering the SCSMIFs from reaching their ultimate capacity. Additionally, it can marginally impair ductility by reducing Δ_u (DI) up to 13% (4%). This is because premature instability can reduce the ability to deform plastically, leading to reduced ductility, as shown in **Supplementary Figure B1(b)**. This highlights the significance of maintaining sufficient ductility for effective energy dissipation and resilience of SCSMIF under severe load conditions.

5.3 Columns lengths (L_c)

Figure 17(c) reveals that elongating the columns from 0.6 to 1.2 and 3 m for a given L_{FB} and L_{CB} of 0.6, 1.2, and 3 m, D_{FB}, D_{CB}, B_{FB}, and B_{CB} of 150 and 200 mm, and t_{FB} and t_{CB} of 8 mm while keeping other members constant can impair the frames' compressive behavior by decreasing P_u (K_e) up to 68% (76%). This is because longer columns become more slender, reducing their resistance to buckling and bending and increasing deflection and bending stresses, lowering the overall load-carrying capacity of SCSMIFs. It can increase Δ_u by up to 105% due to force redistribution, allowing for more lateral deflection before approaching the buckling limit, as seen in **Supplementary Figure B1(c).** This highlights the need for careful column length selection in coordination with other members during design.

5.4 Columns cross-sections (D_c×B_c)

Figure 17 (d) indicates that, while keeping other members constant, increasing the column cross-sections from 150 to 180, 200, and 210 mm for a given L_c, L_{FB}, and L_{CB} of 1.2, 2.5, and 3.6 m and t_c, t_{FB}, and t_{CB} of 8 mm can improve SCSMIF compressive performance by raising their P_u (K_e) by up to 155% (116%). However, it might also have adverse effects as it can lower Δ_u (DI) by as much as 16% (41%). Increased D_c and B_c improve the columns' resistance to buckling and bending and reduce their slenderness, strengthening SCSMIFs. However, increasing D_c/t_c, as shown in **Supplementary Figure B1(d)**, reduces the frame members' flexibility, lowers buckling strain, and diminishes the SCSMIFs' ductility.

5.5 Columns thickness (t_c)

As depicted in **Fig. 17(e)**, column thickness variations can influence the compression behavior of SCSMIFs. Results indicate that increasing the thickness of the cross-section of columns from 6 to 8 and 10 mm for a given D_c and B_c of 150, 180, 200, and 210 mm can enhance the performance of SCSMIFs by increasing their P_u (K_e) by up to 188% (93%) and Δ_u (DI) by up to 60% (96%). This is a result of the reduction in D_c/t_c, which increases the buckling and bending resistance of the columns while decreasing their slenderness. **Supplementary Figure B1(e)** reveals that SCSMIFs can withstand more significant plastic deformations before failure, ultimately increasing their compressive strength, buckling strain, and ductility. This emphasizes the importance of considering column dimensions carefully during SCSMIFs' design for robust and resilient MSBs.

5.6 Beams gap, connecting plate thickness, and columns gap

Supplementary Table A1 and **Figs. 17(f~h)** and **Supplementary Figure B1(f,g,k)** demonstrate that as long as the SCSMIFs retain the stiffness of members and IMCs per the prototype design, limited increases in the gap between beams (from 20 to 74 and 133 mm), the thickness of the connecting plate (from 5 to 15 and 30 mm), and the gap between columns (from 12 to 24 and 36 mm) do not have a significant impact on the compressive behavior of SCSMIFs. They resulted in a maximum 3% decrease in strength. Columns in SCSMIFs are capable of withstanding compressive forces, preventing excessive deformation or local buckling of other members. Despite the impact of modular gaps on lateral stability, SCSMIFs can still resist compressive forces. Moreover, increasing the gap between columns increases the ductility by up to 2%, allowing lateral movement. These findings demonstrate that rotary-type IMCs transfer compressive stresses effectively, preserving the integrity of SCSMIFs [27,88].

5.7 Columns quantity

Figures 17(i) and **19(a~d)** illustrate the P-Δ curves and failure modes, highlighting that P_u and K_e improve linearly as the column number increases from 1 to 2, 3, and 4. For given D_{FB} and D_{CB} (150 mm), B_{FB} and B_{CB} (200 and 150 mm), and varying t_{FB} and t_{CB}

(8 and 6 mm), P_u (K_e) raises by 193% (142%), 345% (264%), 482% (384%) and 191% (132%), 341% (251%), 477% (367%). The relationship between Δ_u is less pronounced due to data fluctuation. However, *DI* is significantly reduced by up to 38% and 40%. The substantial increase in P_u by 2.9, 4.4, and 5.8 times, and K_e by 2.3, 3.5, and 4.7 times confirms the positive effect of members' grouping. Increasing the number of columns enhances the compressive behavior of the SCSMIF by more than 2, 3, and 4 times when advancing from a single to a double, triple, or quadruple-grouped frame skeleton. The failure mode remains on the lower end of the upper columns, indicating that increasing the number of frame skeletons distributes the load, reduces the stress on individual components, and increases the overall capacity of the SCSMIF without altering the failure pattern.

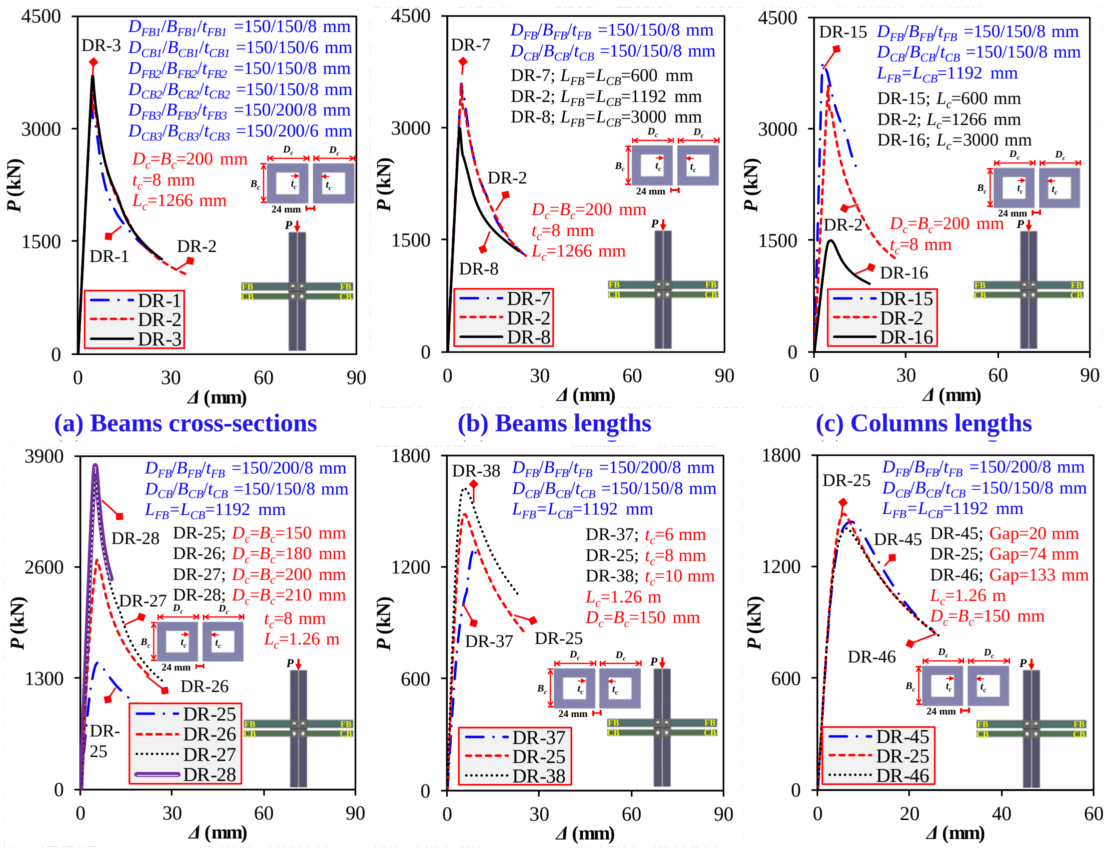

(a) Beams cross-sections (b) Beams lengths (c) Columns lengths

(d) Columns cross-sections (e) Columns thickness (f) Beams gap

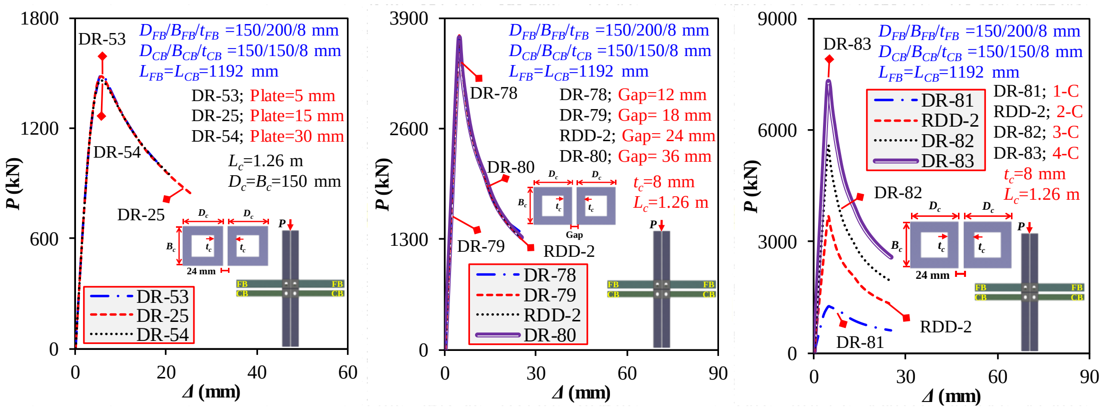

(g) Connecting plate thickness **(h) Columns gap** **(i) Columns quantity**

Fig. 17 Influence of varying parameters on typical load-shortening curves

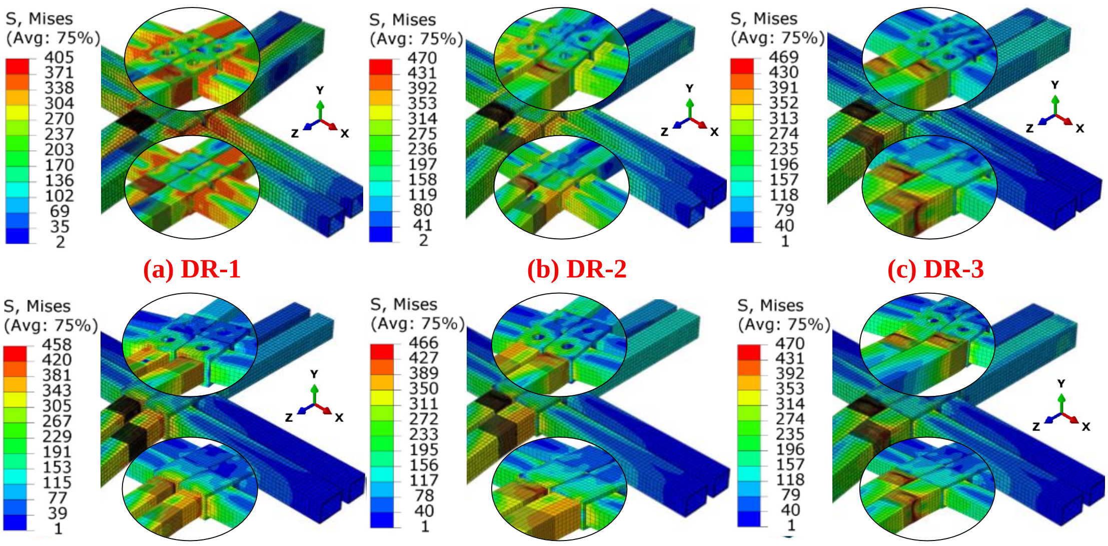

(a) DR-1 **(b) DR-2** **(c) DR-3**

(d) DR-25 **(e) DR-26** **(f) DR-27**

Fig. 18 Typical failure modes SCSMIFs under compression

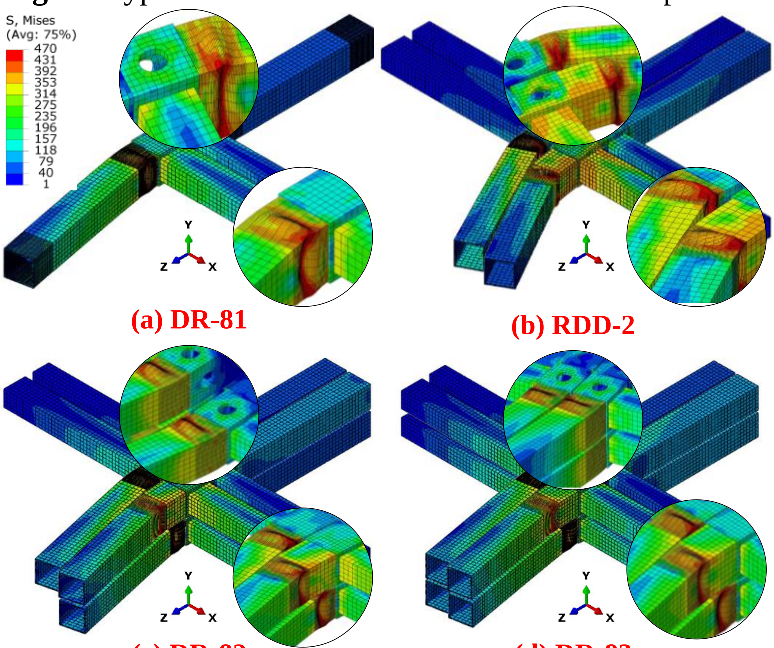

(a) DR-81 **(b) RDD-2**

(c) DR-82 **(d) DR-83**

Fig. 19 Influence of varying column quantity on failure modes of SCSMIFs

6 Theoretical investigation of buckling load for rotary-connected SCSMIFs

The observed failure mechanism disclosed an S-shaped pattern marked by local inward and outward buckling, exhibiting both elastic and plastic failure modes. It reveals that the upper columns did not satisfy the EC3 Class 3 slenderness requirements, as elastic buckling was not permitted, stopping the cross-section from achieving complete yielding. Local buckling is believed to substantially affect the cross-sectional and member capacities, regardless of whether inelastic or elastic [6]. Therefore, global strength accounting for the radius of gyration, elastic buckling stress, and strength reduction under these conditions produces more conservative results than the cross-sectional strength [66]. Identical design practices were observed in other studies, like Refs. [119,120] employed global strength prediction equations for member design, taking yield strength failure with local buckling of Class 3 steel columns into account. Ref. [121] used local buckling reduction factors for fixed-ended short columns. Moreover, the member buckling strength was the primary design strength criterion used in Ref. [122]. In addition, the global buckling strength model was applied to simple-supported, concentrically compressed members in Ref. [123]. According to IS800 [54,55], NZS 3404[56], EC3:1-1 [57], CSA S16-19 [58], AISC360-16 [59], and GB 50017-2017 [60], the effective length factor played a crucial role in stability design, which was dependent on the degree of elastic restraint at the column's ends. Because MSB columns have semi-rigid connections at their ends, making them unique. Therefore, their effective length factor and buckling load vary based on the relative joint and member bending stiffness ratio and the rigidity of vertical and horizontal IMCs. Considering the global strength rather than the cross-sectional strength is always preferred to account for these factors effectively [49]. Thus, it is reasonable to determine the buckling strength to account for the local elastic and plastic buckling.

Chen et al. [70], further highlighted that insufficient connection stiffness would result in a greater slenderness of the MSB columns, highlighting the need for stability analysis to evaluate buckling performance and determine influential design factors for columns in MSBs. Therefore, the stability design methods have utilized the SCSMIFs' global strength to achieve a buckling load more conservatively than a cross-section resistance design.

Assuming the ITCs are fixed, the sub-assembled SCSMIFs shown in **Fig. 20(a)** were analyzed for buckling load using three-story full-scale models in **Fig. 20(b)**. Pin and semi-rigid IMCs were employed, along with stability functions from Eqns—1 and 2 introduced in Ref. [124] and buckling load from Eqn. 3 in Ref. [83].

$$S_{ii} = \frac{\left(\frac{\pi}{\mu}\right)^2 - \frac{\pi}{\mu}\sin\frac{\pi}{\mu}}{2 - 2\cos\frac{\pi}{\mu} - \frac{\pi}{\mu}\sin\frac{\pi}{\mu}}\ ;\ S_{ij} = \frac{\frac{\pi}{\mu}\sin\frac{\pi}{\mu} - \left(\frac{\pi}{\mu}\right)^2\cos\frac{\pi}{\mu}}{2 - 2\cos\frac{\pi}{\mu} - \frac{\pi}{\mu}\sin\frac{\pi}{\mu}} \quad \text{for } \mathrm{c}_1, \mathrm{c}_2, \mathrm{c}_3, \mathrm{c}_4, \mathrm{c}_5, \text{and } \mathrm{c}_6 \tag{1}$$

$$S_{ii} = 4\ ;\ S_{ij} = 2 \quad \text{for } \mathrm{b}_1, \mathrm{b}_2, \mathrm{b}_3, \mathrm{b}_4, \mathrm{b}_5, \mathrm{b}_6, \mathrm{b}_7, \text{and } \mathrm{b}_8 \tag{2}$$

$$P_{cr} = \left[\pi^2 EI_{c2} / (2\mu L_{ct})^2\right] \tag{3}$$

6.1 Pinned IMCs

The moments in each member via Eqns. 4~7 and their equilibrium at joints A, B, and sway for the target column c_2 in **Fig. 20(c)** are determined using Eqn. 8 according to Chen et al.'s model [83] as follows:

$$(M_A)_{c2} = \left(EI_{c2}/L_{c2}\right)\left[S_{ii}\theta_A + S_{ij}\theta_B - \left(S_{ii} + S_{ij}\right)\Delta_c/L_{ct}\right] \tag{4}$$

$$(M_B)_{c2} = \left(EI_{c2}/L_{c2}\right)\left[S_{ij}\theta_A + S_{ii}\theta_B - \left(S_{ii} + S_{ij}\right)\Delta_c/L_{ct}\right] \tag{5}$$

$$(M_A)_{b2} = \left(EI_{b2}/L_{b2}\right)[4\theta_A + 2\theta_B] = \left(EI_{b2}/L_{b2}\right)[6\theta_A] \tag{6}$$

$$(M_B)_{b3} = \left(EI_{b3}/L_{b3}\right)[4\theta_B + 2\theta_A] = \left(EI_{b3}/L_{b3}\right)[6\theta_B] \tag{7}$$

$$(M_A)_{c2} + (M_A)_{b2} = 0; (M_B)_{c2} + (M_B)_{b3} = 0;\ (M_A)_{c2} + (M_B)_{c2} + P\Delta_c = 0 \tag{8}$$

$$\theta_A(S_{ii} + 6G_C) + \theta_B\left(S_{ij}\right) + \Delta_c/L_{ct}\left[-\left(S_{ii} + S_{ij}\right)\right] = 0\ ;\ G_C = \frac{EI_{b2}/L_{b2}}{EI_{c2}/L_{ct}} \tag{9}$$

$$\theta_A\left(S_{ij}\right) + \theta_B(S_{ii} + 6G_D) + \Delta_c/L_{ct}\left[-\left(S_{ii} + S_{ij}\right)\right] = 0;\ G_D = \frac{EI_{b3}/L_{b3}}{EI_{c2}/L_{ct}} \tag{10}$$

$$\theta_A\left(S_{ii} + S_{ij}\right) + \theta_B\left(S_{ii} + S_{ij}\right) - \Delta_c/L_{ct}\left[2\left(S_{ii} + S_{ij}\right) - \left(\pi^2/\mu^2\right)\right] = 0 \tag{11}$$

where $P = \frac{\pi^2 EI_{c2}}{\mu^2 L_{c2}{}^2}$. By solving Eqns. 9~11 using a determinant, μ is calculated from Eqn. 12 and then substituted in Eqn. 3 to obtain the buckling load (P_{cr}/PD) of a pinned sub-assembled rotary-connected SCSMIF.

$$\begin{aligned}(S_{ii}+6G_C)&\left[\left\{\left({\pi^2}/{\mu^2}\right)-2\left(S_{ii}+S_{ij}\right)\right\}\times\{S_{ii}+6G_D\}+(S_{ii}+S_{ij})^2\right]\\&-\left(S_{ij}\right)\left[\{S_{ij}\}\times\left\{\left({\pi^2}/{\mu^2}\right)-2\left(S_{ii}+S_{ij}\right)\right\}+(S_{ii}+S_{ij})^2\right]\\&-\left(S_{ii}+S_{ij}\right)\left[(S_{ij})\times(S_{ii}+S_{ij})\;-(S_{ii}+S_{ij})\;\times(S_{ii}+6G_D)\right]=0\end{aligned} \tag{12}$$

6.2 Semi-rigid IMCs

6.2.1 Vertical rotary-type IMCs

According to Li et al.'s model [76], the rotary-connected SCSMIFs shown in **Fig. 20(d)** experience double curvature bending, which results in equal beam end rotations, i.e., $\theta_B = \theta_G$; $\theta_C = \theta_H$; $\theta_D = \theta_I$; $\theta_E = \theta_J$. Additionally, the column end rotations are given by $\theta_A = \theta_C - \frac{M_B}{R_{1v}} \times \frac{\theta_D}{\theta_C}$, $\theta_B = \theta_G = \theta_C - \frac{M_B}{R_{1v}}$, $\theta_E = \theta_J = \theta_D - \frac{M_E}{R_{2v}}$, and $\theta_F = \theta_D - \frac{M_E}{R_{2v}} \times \frac{\theta_C}{\theta_D}$. The moments of the members can be determined via Eqns. 13~20 using slope-deflection equations as follows:

$$(M_{BA})_{c1} = {EI_{c1}}/{L_{ct}}\left[S_{ii}\left(\theta_C-\frac{M_B}{R_{1v}}\right)+S_{ij}\left(\theta_D-\frac{M_B}{R_{1v}}\times\frac{\theta_D}{\theta_C}\right)-\left(S_{ii}+S_{ij}\right){\Delta_c}/{L_{ct}}\right] \tag{13}$$

$$(M_{CD})_{c2} = {EI_{c2}}/{L_{ct}}\left[S_{ii}\theta_C+S_{ij}\theta_D-\left(S_{ii}+S_{ij}\right){\Delta_c}/{L_{ct}}\right] \tag{14}$$

$$(M_{DC})_{c2} = {EI_{c2}}/{L_{ct}}\left[S_{ii}\theta_D+S_{ij}\theta_C-\left(S_{ii}+S_{ij}\right){\Delta_c}/{L_{ct}}\right] \tag{15}$$

$$(M_{EF})_{c3} = {EI_{c3}}/{L_{ct}}\left[S_{ii}\left(\theta_D-\frac{M_E}{R_{2v}}\right)+S_{ij}\left(\theta_C-\frac{M_E}{R_{2v}}\times\frac{\theta_C}{\theta_D}\right)-\left(S_{ii}+S_{ij}\right){\Delta_c}/{L_{ct}}\right] \tag{16}$$

$$(M_{BG})_{b1} = 6\left({EI_{b1}}/{L_{b1}}\right)\theta_B = 6\left({EI_{b1}}/{L_{b1}}\right)\left(\theta_C-\frac{M_B}{R_{1v}}\right) \tag{17}$$

$$(M_{CH})_{b2} = 6\left({EI_{b2}}/{L_{b2}}\right)\theta_C \tag{18}$$

$$(M_{DI})_{b3} = 6\left({EI_{b3}}/{L_{b3}}\right)\theta_D \tag{19}$$

$$\left(M_{EJ}\right)_{b4} = 6\left({EI_{b4}}/{L_{b4}}\right)\theta_E = 6\left({EI_{b4}}/{L_{b4}}\right)\left(\theta_D-\frac{M_E}{R_{2v}}\right) \tag{20}$$

The equilibrium of moments at joints C and D and the sway can be determined by considering c_2 as the objective column, using Eqns. 21 to 23, as shown below:

$$(M_{BA})_{c1}+(M_{BG})_{b1}+(M_{CH})_{b2}+(M_{CD})_{c2}=0 \tag{21}$$

$$(M_{EF})_{c3}+\left(M_{EJ}\right)_{b4}+(M_{DI})_{b3}+(M_{DC})_{c2}=0 \tag{22}$$

$$(M_{CD})_{c2}+(M_{DC})_{c2}+P\Delta_c=0 \tag{23}$$

When $P=\frac{\pi^2 EI_{c2}}{\mu^2 L_{c2}{}^2}$ is substituted into Eqn. 23, the resulting equation enables the calculation of ${}^{\Delta_c}/_{L_{ct}}=\frac{\mu^2(S_{ii}+S_{ij})(\theta_C+\theta_D)}{-\pi^2+2(S_{ii}+S_{ij})\mu^2}$. Introducing ${}^{\Delta_c}/_{L_{ct}}$, the equations (Eqns. 13~20), the relative members', i.e., $G_{1v}=\frac{EI_{b1}/L_{b1}}{EI_{c1}/L_{ct}}, G_{2v}=\frac{EI_{b2}/L_{b2}}{EI_{c2}/L_{ct}}, G_{3v}=\frac{EI_{b3}/L_{b3}}{EI_{c2}/L_{ct}}, G_{4v}=\frac{EI_{b4}/L_{b4}}{EI_{c3}/L_{ct}}$, and the IMC-to-members stiffnesses ratios, i.e., $J_{1v}=\frac{R_{1v}}{EI_{c1}/L_{ct}}, J_{2v}=\frac{R_{1v}}{EI_{c2}/L_{ct}}, J_{3v}=\frac{R_{2v}}{EI_{c2}/L_{ct}}, J_{4v}=\frac{R_{2v}}{EI_{c3}/L_{ct}}$ into Eqns. 21 and 22. Then, by rearranging the equations in terms of $\theta_C{}^2$, $\theta_D{}^2$, and $\theta_C\theta_D$, the resulting equations (Eqns. 24 and 25) are obtained.

$$\theta_C{}^2\Big[(6G_{1v}+S_{ii})(6G_{2v}+S_{ii})+(6G_{1v}J_{2v}+6G_{2v}J_{1v}+S_{ii}J_{2v}+S_{ii}J_{1v})-\frac{\mu^2}{-\pi^2+2(S_{ii}+S_{ij})\mu^2}(6G_{1v}+S_{ii}+J_{1v}+J_{2v})(S_{ii}+S_{ij})^2\Big]+\theta_D{}^2\Big[S_{ij}{}^2-\frac{\mu^2}{-\pi^2+2(S_{ii}+S_{ij})\mu^2}S_{ij}(S_{ii}+S_{ij})^2\Big]+\theta_C\theta_D\Big[S_{ij}(J_{2v}+J_{1v}+6G_{2v}+2S_{ii}+6G_{1v})-\frac{\mu^2}{-\pi^2+2(S_{ii}+S_{ij})\mu^2}(6G_{1v}+S_{ii}+J_{1v}+J_{2v})(S_{ii}+S_{ij})^2-\frac{\mu^2}{-\pi^2+2(S_{ii}+S_{ij})\mu^2}S_{ij}(S_{ii}+S_{ij})^2\Big]=0 \tag{24}$$

$$\theta_D{}^2\Big[(6G_{3v}+S_{ii})(6G_{4v}+S_{ii})+(6G_{4v}J_{3v}+6G_{3v}J_{4v}+S_{ii}J_{4v}+S_{ii}J_{3v})-\frac{\mu^2}{-\pi^2+2(S_{ii}+S_{ij})\mu^2}(6G_{4v}+S_{ii}+J_{4v}+J_{3v})(S_{ii}+S_{ij})^2\Big]+\theta_C{}^2\Big[S_{ij}{}^2-\frac{\mu^2}{-\pi^2+2(S_{ii}+S_{ij})\mu^2}S_{ij}(S_{ii}+S_{ij})^2\Big]+\theta_C\theta_D\Big[S_{ij}(J_{3v}+J_{4v}+6G_{3v}+2S_{ii}+6G_{4v})-\frac{\mu^2}{-\pi^2+2(S_{ii}+S_{ij})\mu^2}(6G_{4v}+S_{ii}+J_{4v}+J_{3v})(S_{ii}+S_{ij})^2-\frac{\mu^2}{-\pi^2+2(S_{ii}+S_{ij})\mu^2}S_{ij}(S_{ii}+S_{ij})^2\Big]=0 \tag{25}$$

$$(\theta_C+\beta_1\theta_D)(\beta_2\theta_C+\beta_3\theta_D)=0;\ (\beta_4\theta_C+\theta_D)(\beta_5\theta_C+\beta_6\theta_D)=0 \tag{26}$$

Eqn. 26 provides a simplified version of Eqns. 24 and 25, which yield four possible general solutions: $\begin{vmatrix}1 & \beta_1\\ \beta_4 & 1\end{vmatrix}=0, \begin{vmatrix}1 & \beta_1\\ \beta_5 & \beta_6\end{vmatrix}=0, \begin{vmatrix}\beta_2 & \beta_3\\ \beta_4 & 1\end{vmatrix}=0$, and $\begin{vmatrix}\beta_2 & \beta_3\\ \beta_5 & \beta_6\end{vmatrix}=0$. These general solutions are utilized to obtain the simplified expressions presented in Eqns. 27~30 after solving the determinant. The maximum value obtained from Eqns. 27~30 determines the maximum μ value, which is then inserted into Eqn. 3 to calculate the minimum buckling load (P_{cr}/SR) of a sub-assembled rotary-connected SCSMIF with vertical IMC.

$$1-\left[\frac{2[S_{ij}{}^2-D]}{[S_{ij}(E)-C-D]+\sqrt{[S_{ij}(E)-C-D]^2-4[S_{ij}{}^2-D][A+B-C]}}\right]\left[\frac{2[S_{ij}{}^2-I]}{[S_{ij}J-H-I]+\sqrt{[S_{ij}J-H-I]^2-4[F+G-H][S_{ij}{}^2-I]}}\right]=0 \tag{27}$$

$$[F+G-H]-\left[\frac{2\left[S_{ij}{}^{2}-D\right]}{\left[S_{ij}(E)-C-D\right]+\sqrt{\left[S_{ij}(E)-C-D\right]^{2}-4\left[S_{ij}{}^{2}-D\right][A+B-C]}}\right]\left[\frac{\left[S_{ij}J-H-I\right]+\sqrt{\left[S_{ij}J-H-I\right]^{2}-4[F+G-H]\left[S_{ij}{}^{2}-I\right]}}{2}\right]=0 \tag{28}$$

$$[A+B-C]-\left[\frac{\left[S_{ij}(E)-C-D\right]+\sqrt{\left[S_{ij}(E)-C-D\right]^{2}-4\left[S_{ij}{}^{2}-D\right][A+B-C]}}{2}\right]\left[\frac{2\left[S_{ij}{}^{2}-I\right]}{\left[S_{ij}J-H-I\right]+\sqrt{\left[S_{ij}J-H-I\right]^{2}-4[F+G-H]\left[S_{ij}{}^{2}-I\right]}}\right]=0 \tag{29}$$

$$[A+B-C][F+G-H]-\left[\frac{\left[S_{ij}(E)-C-D\right]+\sqrt{\left[S_{ij}(E)-C-D\right]^{2}-4\left[S_{ij}{}^{2}-D\right][A+B-C]}}{2}\right]\left[\frac{\left[S_{ij}J-H-I\right]+\sqrt{\left[S_{ij}J-H-I\right]^{2}-4[F+G-H]\left[S_{ij}{}^{2}-I\right]}}{2}\right]=0 \tag{30}$$

Coefficients *A*, *B*, *C*, *D*, *E*, *F*, *G*, and *H* are obtained from Eqns. 31~34, which are defined in terms of $\theta_C{}^2$, $\theta_D{}^2$, and $\theta_C\theta_D$ in Eqns. 24 and 25. The value of $R_{1v}=R_{2v}$ =2391.49 kNm/rad is the rotational stiffness of a rotary-type IMC, as stated in Refs. [9].

$$A=(6G_{1v}+S_{ii})(6G_{2v}+S_{ii});\ B=(6G_{1v}J_{2v}+6G_{2v}J_{1v}+S_{ii}J_{2v}+S_{ii}J_{1v}) \tag{31}$$

$$C=\frac{\mu^2(6G_{1v}+S_{ii}+J_{1v}+J_{2v})\left(S_{ii}+S_{ij}\right)^2}{-\pi^2+2\left(S_{ii}+S_{ij}\right)\mu^2};\ D=\frac{\mu^2S_{ij}\left(S_{ii}+S_{ij}\right)^2}{-\pi^2+2\left(S_{ii}+S_{ij}\right)\mu^2} \tag{32}$$

$$E=(J_{2v}+J_{1v}+6G_{2v}+2S_{ii}+6G_{1v});\ F=(6G_{3v}+S_{ii})(6G_{4v}+S_{ii}) \tag{33}$$

$$G=(6G_{4v}J_{3v}+6G_{3v}J_{4v}+S_{ii}J_{4v}+S_{ii}J_{3v});\ H=\frac{\mu^2(6G_{4v}+S_{ii}+J_{4v}+J_{3v})\left(S_{ii}+S_{ij}\right)^2}{-\pi^2+2\left(S_{ii}+S_{ij}\right)\mu^2} \tag{34}$$

6.2.2 Horizontal rotary-type IMCs

In order to find the impact of adjacent module members' and horizontal IMCs' stiffness per Li et al.'s model [76], the end rotations of beams are equal, specifically $\theta_L=\theta_Q$; $\theta_M=\theta_R$; $\theta_N=\theta_S$; $\theta_O=\theta_T$. Addditionally, column end rotations are $\theta_M=\theta_C+\frac{M_C}{R_{1h}}$, $\theta_N=\theta_D-\frac{M_D}{R_{2h}}$. Moments of the members can be expressed with slope-deflection equations using Eqns. 35~37 as follows:

$$(M_{MR})_{b6}=6\left({}^{EI_{b6}}/_{L_{b6}}\right)\left(\theta_C+{}^{M_C}/_{R_{1h}}\right) \tag{35}$$

$$(M_{NS})_{b7}=6\left({}^{EI_{b7}}/_{L_{b7}}\right)\left(\theta_D+{}^{M_D}/_{R_{2h}}\right) \tag{36}$$

$$(M_{MN})_{c5}={}^{EI_{c5}}/_{L_{ct}}\left[S_{ii}\left(\theta_C+{}^{M_C}/_{R_{1h}}\right)+S_{ij}\left(\theta_D+{}^{M_D}/_{R_{2h}}\right)-\left(S_{ii}+S_{ij}\right){}^{\Delta_c}/_{L_{ct}}\right] \tag{37}$$

As depicted in **Fig. 20(d)**, when c_5 is selected as the objective column, the moments' equilibrium at joints M and N can be determined through Eqns. 38 and 39 as follows:

$$(M_{MR})_{b6}+(M_{MN})_{c5}+(M_{CH})_{b2}+(M_{CD})_{c2}=0 \tag{38}$$

$$(M_{MN})_{c5} + (M_{NS})_{b7} + (M_{DC})_{c2} + (M_{DI})_{b3} = 0 \quad (39)$$

By inputting ${}^{\Delta_c}/_{L_{ct}} = \frac{\mu^2(S_{ii}+S_{ij})(\theta_C+\theta_D)}{-\pi^2+2(S_{ii}+S_{ij})\mu^2}$ obtained from Eqn. 23, along with members' relative stiffness ratios, such as $G_{1h} = \frac{EI_{b6}/L_{b6}}{EI_{c5}/L_{ct}}, G_{2h} = \frac{EI_{b7}/L_{b7}}{EI_{c5}/L_{ct}}, G_{2v} = \frac{EI_{b2}/L_{b2}}{EI_{c2}/L_{ct}}, G_{3v} = \frac{EI_{b3}/L_{b3}}{EI_{c2}/L_{ct}}$, and $K = \frac{EI_{c2}/L_{ct}}{EI_{c5}/L_{ct}}$, and the IMC-to-member relative stiffness ratios, i.e., $J_{1h} = \frac{R_{1h}}{EI_{c2}/L_{ct}}$ and $J_{2h} = \frac{R_{2h}}{EI_{c5}/L_{ct}}$ into Eqns. 38 and 39, it is possible to rearrange equations in terms of θ_C and θ_D to obtain Eqns. 40 and 41.

$$\begin{aligned}\theta_C \Big[&J_{Ih}J_{2h}(6G_{1h} + S_{ii} + 6G_{2v}K + KS_{ii}) + J_{2h}\big(36G_{1h}G_{2v} + 6G_{1h}S_{ii} + 6G_{2v}S_{ii} + {S_{ii}}^2\big) - J_{Ih}{S_{ij}}^2 - \frac{\mu^2(S_{ii}+S_{ij})}{-\pi^2+2(S_{ii}+S_{ij})\mu^2}\{J_{Ih}J_{2h}\big(S_{ii} + S_{ij} + KS_{ii} + KS_{ij}\big) + J_{2h}\big(6G_{1h}S_{ii} + \\ &6G_{1h}S_{ij} + {S_{ii}}^2\big) + S_{ii}S_{ij}(J_{2h} - J_{1h}) - J_{1h}{S_{ij}}^2\}\Big] + \theta_D \Big[J_{Ih}J_{2h}S_{ij}(1 + K) + \\ &J_{2h}S_{ij}(6G_{1h} + S_{ii}) - J_{Ih}S_{ij}(6G_{3v} - S_{ii}) - \frac{\mu^2(S_{ii}+S_{ij})}{-\pi^2+2(S_{ii}+S_{ij})\mu^2}\{J_{Ih}J_{2h}\big(S_{ii} + S_{ij} + \\ &KS_{ii} + KS_{ij}\big) + J_{2h}\big(6G_{1h}S_{ii} + 6G_{1h}S_{ij} + {S_{ii}}^2\big) + S_{ii}S_{ij}(J_{2h} - J_{1h}) - J_{Ih}{S_{ij}}^2\}\Big] = 0\end{aligned} \quad (40)$$

$$\begin{aligned}\theta_C \Big[&J_{Ih}J_{2h}(1 + K)S_{ij} + J_{2h}S_{ij}(6G_{2v} + S_{ii}) - J_{Ih}S_{ij}(S_{ii} + 6G_{2h}) - \\ &\frac{\mu^2(S_{ii}+S_{ij})}{-\pi^2+2(S_{ii}+S_{ij})\mu^2}\{J_{Ih}J_{2h}\big(S_{ii} + S_{ij} + KS_{ii} + KS_{ij}\big) - J_{Ih}\big({S_{ii}}^2 + 6S_{ii}G_{2h} + 6S_{ij}G_{2h}\big) + \\ &J_{2h}\big({S_{ij}}^2\big) + S_{ii}S_{ij}(J_{2h} - J_{1h})\}\Big] + \theta_D \Big[J_{Ih}J_{2h}(S_{ii} + 6G_{2h} + 6KG_{3v} + KS_{ii}) - \\ &J_{Ih}\big(6G_{3v}S_{ii} + {S_{ii}}^2 + 36G_{3v}G_{2h} + 6S_{ii}G_{2h}\big) + J_{2h}{S_{ij}}^2 - \\ &\frac{\mu^2(S_{ii}+S_{ij})}{-\pi^2+2(S_{ii}+S_{ij})\mu^2}\{J_{Ih}J_{2h}\big(S_{ii} + S_{ij} + KS_{ii} + KS_{ij}\big) - J_{Ih}\big({S_{ii}}^2 + 6S_{ii}G_{2h} + 6S_{ij}G_{2h}\big) + \\ &J_{2h}\big({S_{ij}}^2\big) + S_{ii}S_{ij}(J_{2h} - J_{1h})\}\Big] = 0\end{aligned} \quad (41)$$

$$\theta_C[\xi_1] + \theta_D[\xi_2] = 0;\ \theta_C[\beta_3] + \theta_D[\beta_4] = 0 \quad (42)$$

Eqn. 42 is a simplified form of Eqns. 40 and 41, and its general solution is $\begin{vmatrix}\xi_1 & \xi_2 \\ \xi_3 & \xi_4\end{vmatrix} = 0$. After determining the general solution using Eqn. 42, the μ value can be obtained and then inserted into Eqn. 3 to calculate the buckling load (P_{cr}/SR) of a sub-assembled SCSMIF considering horizontal IMCs and adjacent modular frame members stiffnesses effect.The coefficients ξ_1, ξ_2, ξ_3, and ξ_4 are derived from Eqns. 43~46, which are expressed in terms of θ_C and θ_D as defined in Eqns. 40 and 41.

$$\begin{aligned}\xi_1 = &J_{Ih}J_{2h}(6G_{1h} + S_{ii} + 6G_{2v}K + KS_{ii}) \\ &+ J_{2h}\big(36G_{1h}G_{2v} + 6G_{1h}S_{ii} + 6G_{2v}S_{ii} + {S_{ii}}^2\big) - J_{Ih}{S_{ij}}^2 - Z_1\end{aligned} \quad (43)$$

$$\xi_2 = J_{Ih}J_{2h}S_{ij}(1+K) + J_{2h}S_{ij}(6G_{1h}+S_{ii}) - J_{Ih}S_{ij}(6G_{3v}-S_{ii}) - Z_1 \tag{44}$$

$$\xi_3 = J_{Ih}J_{2h}(1+K)S_{ij} + J_{2h}S_{ij}(6G_{2v}+S_{ii}) - J_{Ih}S_{ij}(S_{ii}+6G_{2h}) - Z_2 \tag{45}$$

$$\begin{aligned}\xi_4 = {} & J_{Ih}J_{2h}(S_{ii}+6G_{2h}+6KG_{3v}+KS_{ii}) \\ & - J_{Ih}\left(6G_{3v}S_{ii}+{S_{ii}}^2+36G_{3v}G_{2h}+6S_{ii}G_{2h}\right) + J_{2h}{S_{ij}}^2 - Z_2\end{aligned} \tag{46}$$

$$\begin{aligned}Z_1 = {} & \frac{\mu^2\left(S_{ii}+S_{ij}\right)}{-\pi^2+2\left(S_{ii}+S_{ij}\right)\mu^2}\left\{J_{Ih}J_{2h}\left(S_{ii}+S_{ij}+KS_{ii}+KS_{ij}\right)\right. \\ & \left. + J_{2h}\left(6G_{1h}S_{ii}+6G_{1h}S_{ij}+{S_{ii}}^2\right) + S_{ii}S_{ij}(J_{2h}-J_{Ih}) - J_{Ih}{S_{ij}}^2\right\}\end{aligned} \tag{47}$$

$$\begin{aligned}Z_2 = {} & \frac{\mu^2\left(S_{ii}+S_{ij}\right)}{-\pi^2+2\left(S_{ii}+S_{ij}\right)\mu^2}\left\{J_{Ih}J_{2h}\left(S_{ii}+S_{ij}+KS_{ii}+KS_{ij}\right)\right. \\ & \left. - J_{Ih}\left({S_{ii}}^2+6S_{ii}G_{2h}+6S_{ij}G_{2h}\right) + J_{2h}\left({S_{ij}}^2\right) + S_{ii}S_{ij}(J_{2h}-J_{Ih})\right\}\end{aligned} \tag{48}$$

The coefficients Z_1 and Z_2 are obtained from Eqns. 47 and 48, and $R_{1h} = R_{2h} =$151 kN/mm represents the shear stiffness of a horizontal rotary-type IMC as given in Refs. [9,40].

6.3 Validations

The details of the FEMs' buckling loads (P_{cr}/FE) are compared with the theoretical results (P_{cr}/PD and P_{cr}/SR) in **Fig. 15(b)** and **Table 2**. P_{cr}/PD represents the buckling load obtained using the pinned IMC's Eqn. 12, while P_{cr}/SR corresponds to the minimum buckling load obtained by solving vertical rotary-type IMCs' Eqn. 26 or horizontal IMCs' Eqn. 42. Based on Refs. [9,40], $R_{1h} = R_{2h}$ is typically lower than other components and vertical IMC rotational stiffness. Consequently, horizontal IMCs' stiffness does not directly impact the buckling behavior, and its μ value has minimal influence on the buckling behavior of SCSMIF. This suggests that the stability of SCSMIF is primarily determined by the members' or the vertical IMC-to-members relative stiffnesses and that adjacent frames behave independently. When the columns are comparatively slender and the members' stiffnesses are lesser than horizontal IMC, it is crucial to consider the effect of the horizontal IMC as it could reduce effective length and increase buckling load. These findings are consistent with tests and literature, indicating that adjacent frame behave independently without any deteriorating impact

[49]. The average (Cov) prediction ratios of the tested and parametric FEMs for P_{cr}/PD and P_{cr}/SR are 0.71(0.05)/0.93(0.05) and 0.69(0.20)/0.95(0.16), offering conservative results. However, P_{cr}/PD had a large scatter and underestimated findings over the larger range, while P_{cr}/SR produced more accurate outcomes with minimal scatter. Additionally, a safety factor could further improve slight overestimations. The results showed that accurately anticipating the compressive behavior of sub-assembled rotary-connected SCSMIFs could be achieved by considering the semi-rigidity and rotational stiffness of rotary-type IMCs, as determined in Refs. [9]. Conversely, assuming rotary-type IMCs to be pinned could not reflect their actual behavior and could result in an uneconomical design.

Assuming pinned IMC results in conservative estimates for the buckling load that applies to all SCSMIFs. On the other hand, considering the semi-rigidity of IMCs yields more accurate predictions for rotary-connected SCSMIFs, including those for exterior, middle, or interior frames. These findings were consistent with tests implying that relative rotation between the upper and lower frame skeleton at rotary-type IMCs cannot be simulated as pinned. However, these outcomes are specific to the models used and require additional validation. Moreover, these results cannot be directly applied to non-sway or special frames with welded IMCs or shear-keyed columns.

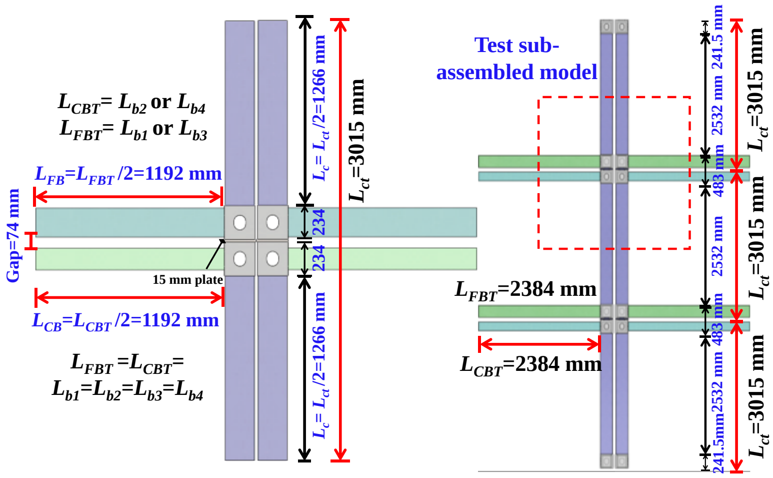

(a) Test sub-assembled model (b) Three-story model

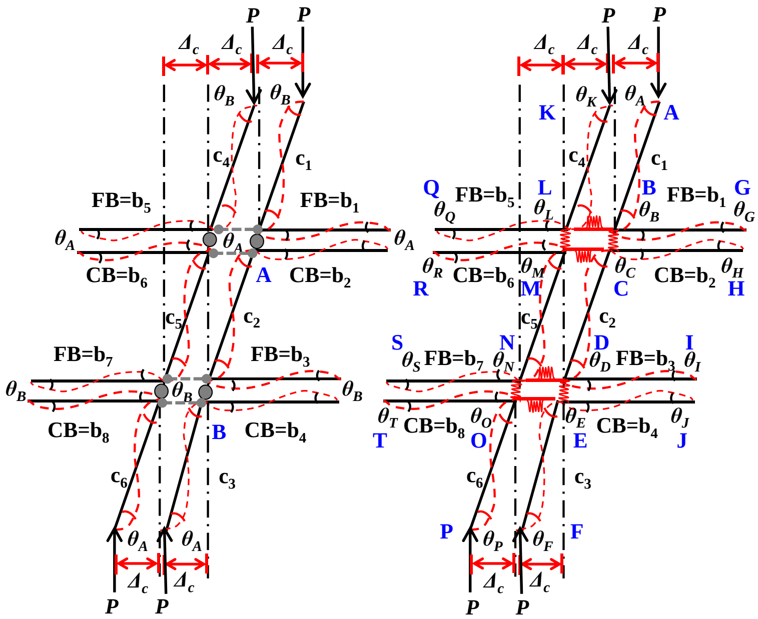

(c) Pinned model (d) Semi-rigid model

Fig. 20 Theoretical buckling load sub-assembled models; Per Chen et al.'s model [83] for pinned and Li et al.'s model [76] for semi-rigid rotary-connected SCSMIFs

7 Design guidelines and recommendations

Experimental, numerical, and theoretical results on the compressive performance of SCSMIFs with rotary-type IMCs add significantly to the structural integrity and stability of MSBs, allowing for conservative and cost-effective design. These results provide valuable insights into modular frame columns' global and local buckling under compression loads, contributing to significant revelations about these structures' failure modes and load-carrying capacity. When incorporating rotary-type IMCs into structural designs, it is essential to count on acquiring precise mechanical properties, such as rotational stiffness, strength, and behavioral characteristics of the vertical and horizontal IMCs from Refs. [9,40]. Selecting structural members with an appropriate cross-sectional dimension or shape and higher rigidity is crucial as this offers greater adaptability for meeting cross-sectional needs. The parametric analysis exposes that the primary strength-enhancing parameter is the cross-sectional sizes and thicknesses of columns and beams and adding more columns or adjacent modules. Moreover, applying IMCs with strengthened geometrical designs could optimize the load-bearing capacity of the structures. Reliable decisions can be made concerning selecting and optimizing the rigidities, geometries, and material properties of structural members and connections to ensure structural integrity and satisfy the building's specific performance requirements. The study generated FEMs and theoretical models to describe the behavior of pinned and semi-rigid IMCs, which were rigorously analyzed and validated using experimental and numerical data, resulting in accurate predictions of buckling loads and potential failure modes. Using these predictive models in the design process permits the identification of problem areas, such as high-stress concentrations or unstable regions, thereby optimizing the design to guarantee the reliability and structural integrity of the MSB. Consideration of the pinned nature produces a large scatter, whereas the semi-rigidity of IMCs yields more precise predictions with less scatter. Nevertheless, it is essential to acknowledge that the semi-rigid behavior of IMCs in modular frames brings significant challenges in their design and can contribute to complexities in modeling and analyzing these structures, which consumes considerable time and resources [80,81]. Complex joint configurations can even result in unpredictable behavior [82]. This study's theoretical models supply a categorization system for pinned and semi-rigid IMCs, which can increase interconnection behavior prediction and modular system dependability. These models are beneficial for navigating the complexities and unpredictability of joint behavior, and they can guide the efficient control of relative stiffnesses for a conservative and cost-effective design. Even though this study provides essential guidance for designing rotary-connected SCSMIFs, other studies can be carried out to compare the performance of different types of IMCs.

8 Conclusions

This study conducted two sub-assembled tests, analyzed 87 parametric FEMs, and developed theoretical buckling models using pinned and semi-rigid IMCs to estimate the buckling load of rotary-connected SCSMIFs. The investigation aimed to understand the compressive behavior of SCSMIFs and their effect on adjacent members. The study resulted in the following findings:

1. The load-shortening of SCSMIFs exhibited elastic, inelastic, and recessional properties. As the compressive resistance increased from yield to ultimate, local buckling on the upper columns primarily occurred from the bending direction towards the adjacent faces of the columns, associated with sway depending on the relative rigidity of the members. After attaining their ultimate strength, capacity decreased, and buckling became more intense.
2. The SCSMIFs displayed symmetrical S-shaped buckling patterns on all upper column faces, occurring on either the top edges or lower areas at 100-200 mm. The buckling pattern was similar on opposite faces but opposite on adjacent faces of nearby columns. Additionally, the inner sides of grouped columns either bulged out or in, resulting in double S-shaped buckling that prevented collisions on the interior sides. However, the degree of sway and buckling location depended on the members' relative stiffness.
3. The strain curves of the SCSMIFs revealed that S-shaped local buckling only occurred on upper adjacent columns at the same location, either inward or outward, symmetrically on opposite sides and oppositely on adjacent sides. The columns in the direction of bending or the opposite direction demonstrated elastic buckling, whereas the other areas showed plastic buckling. Other members and rotary-type IMCs exhibited no yielding, fracturing, or failure, indicating that the upper columns are the primary load-bearing members.

4. Increasing the cross-section of beams and columns improves the compressive resistance of SCSMIFs, but lengthening them impairs. Greater member rigidity can reduce ductility, but a significant difference in the relative stiffness of the beam and column can lead to premature instability. Raising the column number from 1 to 2, 3, and 4 can enhance strength by 2.9, 4.4, and 5.8 times and stiffness by 2.3, 3.5, and 4.7 times. Changes in beam gap, connecting plate thickness, or column gap did not significantly affect the compressive behavior, while rotary-type IMCs sustained loading without failure.
5. With average prediction errors of 1% and 3.2% for P_u and K_e, the developed FEMs with a mesh of 30 mm, local imperfection of $H/600$ or $0.64t_c$, and global imperfection of $e=3D_c/100$ appropriately replicated SCSMIFs compression behavior, demonstrating their ability to identify SCSMIFs' elastoplastic behavior.
6. The mean (Cov) theory-to-FEM buckling loads were 0.70(0.19) and 0.9(0.13) for pinned and semi-rigid SCSMIFs, suggesting that the semi-rigid model is a more accurate predictor of compressive behavior for rotary-connected SCSMIFs, as it produced more precise results with less scatter than the pinned model, which had significant scatter. Non-identical deflections in tests imply a relative rotation between the upper and lower frame skeleton at rotary-type IMCs that can be better simulated as semi-rigid.

This study focused on standard member cross-sections of rotary-connected SCSMIFs, with possible application to other semi-rigid IMCs using their vertical and horizontal IMC stiffnesses or to all types of IMCs with developed pinned models. Future research will investigate simplified FEMs for rotary-connected SCSMIFs based on the findings of this study, utilizing vertical and horizontal IMCs as spring models to design more practical multi-story MSBs.

Acknowledgment

The authors thank the National Natural Science Foundation of China (Grant No. 51978457 and 52008292) for their financial research support.

References

[1] L. Jaillon, C.S. Poon, The evolution of prefabricated residential building systems in Hong Kong: A review of the public and the private sector, Autom. Constr. 18 (2009) 239–248. https://doi.org/10.1016/j.autcon.2008.09.002.

[2] Y. Liu, Z. Chen, J. Liu, Y. Bai, X. Zhong, X. Wang, Lateral stiffness evaluation on corner-supported thin walled modular steel structures, Thin-Walled Struct. 157 (2020) 106967. https://doi.org/10.1016/j.tws.2020.106967.

[3] L.K. Chen, R.P. Yuan, X.J. Ji, X.Y. Lu, J. Xiao, J.B. Tao, X. Kang, X. Li, Z.H. He, S. Quan, L.Z. Jiang, Modular composite building in urgent emergency engineering projects: A case study of accelerated design and construction of Wuhan Thunder God Mountain/Leishenshan hospital to COVID-19 pandemic, Autom. Constr. 124 (2021) 103555. https://doi.org/10.1016/j.autcon.2021.103555.

[4] Z. Chen, K. Khan, A. Khan, K. Javed, J. Liu, Exploration of the multidirectional stability and response of prefabricated volumetric modular steel structures, J. Constr. Steel Res. 184 (2021) 106826. https://doi.org/10.1016/j.jcsr.2021.106826.

[5] D. Corfar, K.D. Tsavdaridis, A comprehensive review and classification of inter-module connections for hot-rolled steel modular building systems, J. Build. Eng. 50 (2022) 104006. https://doi.org/10.1016/j.jobe.2022.104006.

[6] R.M. Lawson, R.G. Ogden, “Hybrid” light steel panel and modular systems, Thin-Walled Struct. 46 (2008) 720–730. https://doi.org/10.1016/j.tws.2008.01.042.

[7] C.G. Mark Lawson, Ray Odgen, Design in Modular Construction Design in Construction, CRC Press Web, 2014.

[8] J. Liu, Z. Chen, Y. Liu, Y. Bai, X. Zhong, Full-scale corner-supported modular steel structures with vertical inter-module connections under cyclic loading, J. Build. Eng. 44 (2021) 103269. https://doi.org/10.1016/j.jobe.2021.103269.

[9] Z. Chen, Y. Liu, X. Zhong, J. Liu, Rotational stiffness of inter-module connection in mid-rise modular steel buildings, Eng. Struct. 196 (2019) 109273. https://doi.org/10.1016/j.engstruct.2019.06.009.

[10] Y. Liu, Z. Chen, J. Liu, X. Zhong, Experimental study on seismic behavior of two-storey modular structure, Steel Compos. Struct. 37 (2020) 273–289. https://doi.org/10.12989/scs.2020.37.3.273.

[11] C.D. Annan, M.A. Youssef, M.H. Ei-Naggar, Effect of directly welded stringer-to-beam connections on the analysis and design of modular steel building floors, Adv. Struct. Eng. 12 (2009) 373–383. https://doi.org/10.1260/136943309788708400.

[12] C.D. Annan, M.A. Youssef, M.H. El Naggar, Experimental evaluation of the seismic performance of modular steel-braced frames, Eng. Struct. 31 (2009) 1435–1446. https://doi.org/10.1016/j.engstruct.2009.02.024.

[13] C.D. Annan, M.A. Youssef, M.H. El Naggar, Seismic vulnerability assessment of modular steel buildings, J. Earthq. Eng. 13 (2009) 1065–1088. https://doi.org/10.1080/13632460902933881.

[14] C. Annan, M.A. Youssef, M.H. El Naggar, A. Dean, Seismic performance of modular steel braced frames, in: Ninth Can. Conf. Earthq. Eng. Ottawa, Ontario, Canada, 2007. https://doi.org/10.13140/2.1.2132.2241.

[15] C. Annan, M.A. Youssef, M.H. El Naggar, A. Dean, Analytical investigation of semi-rigid floor beams connection in modular steel structures, in: 33rd Annu. Gen. Conf. Can. Soc. Civ. Eng.,

2010. https://doi.org/10.13140/2.1.2010.3687.

[16] J. Zhang, J. Zhao, D. Yang, E. Deng, H. Wang, S. Pang, L. Cai, S. Gao, Mechanical-property tests on assembled-type light steel modular house, J. Constr. Steel Res. 168 (2020) 105981. https://doi.org/10.1016/j.jcsr.2020.105981.

[17] J. Zhang, G. Tian, J. Zhao, E. Deng, M. Wen, L. Ye, X. Guo, J. Zhou, S. Wang, X. Xing, Experimental study on seismic performance of the connection for ATLS modular house, J. Constr. Steel Res. 170 (2020) 106118. https://doi.org/10.1016/j.jcsr.2020.106118.

[18] W. Ferdous, Y. Bai, T. Duc, A. Manalo, P. Mendis, New advancements , challenges and opportunities of multi-storey modular buildings – A state-of-the-art review, Eng. Struct. 183 (2019) 883–893. https://doi.org/10.1016/j.engstruct.2019.01.061.

[19] S. Srisangeerthanan, M.J. Hashemi, P. Rajeev, E. Gad, S. Fernando, Review of performance requirements for inter-module connections in multi-story modular buildings, J. Build. Eng. 28 (2020) 101087. https://doi.org/10.1016/j.jobe.2019.101087.

[20] Z. Ye, K. Giriunas, H. Sezen, G. Wu, D. Feng, State-of-the-art review and investigation of structural stability in multi-story modular buildings, J. Build. Eng. 33 (2021) 101844. https://doi.org/10.1016/j.jobe.2020.101844.

[21] E. Deng, L. Zong, Y. Ding, Z. Zhang, J. Zhang, F. Shi, Seismic performance of mid-to-high rise modular steel construction - A critical review, Thin-Walled Struct. 155 (2020) 106924. https://doi.org/10.1016/j.tws.2020.106924.

[22] H. Thai, T. Ngo, B. Uy, A review on modular construction for high-rise buildings, Structures. 28 (2020) 1265–1290. https://doi.org/10.1016/j.istruc.2020.09.070.

[23] A.W. Lacey, W. Chen, H. Hao, K. Bi, Structural response of modular buildings – An overview, J. Build. Eng. 16 (2018) 45–56. https://doi.org/10.1016/j.jobe.2017.12.008.

[24] Y. Wang, J. Xia, R. Ma, B. Xu, T. Wang, Experimental Study on the Flexural Behavior of an Innovative Modular Steel Building Connection with Installed Bolts in the Columns, Appl. Sci. 9 (2019) 3468. https://doi.org/10.3390/app9173468.

[25] A.W. Lacey, W. Chen, H. Hao, K. Bi, Lateral behaviour of modular steel building with simplified models of new inter-module connections, Eng. Struct. 236 (2021) 112103. https://doi.org/10.1016/j.engstruct.2021.112103.

[26] A.W. Lacey, W. Chen, H. Hao, K. Bi, Review of bolted inter-module connections in modular steel buildings, J. Build. Eng. 23 (2019) 207–219. https://doi.org/10.1016/j.jobe.2019.01.035.

[27] Y. Lyu, G. Li, K. Cao, S. Zhai, H. Li, C. Chen, Y. Wang, Behavior of splice connection during transfer of vertical load in full-scale corner-supported modular building, Eng. Struct. 230 (2021) 111698. https://doi.org/10.1016/j.engstruct.2020.111698.

[28] G. Zhang, L. Xu, X. Xie, Haunch connecting techniques in a self-centering modular steel structure connection system, J. Build. Eng. 62 (2022) 105389. https://doi.org/10.1016/j.jobe.2022.105389.

[29] R. Ma, J. Xia, H. Chang, B. Xu, L. Zhang, Experimental and numerical investigation of mechanical properties on novel modular connections with superimposed beams, Eng. Struct. J. 232 (2021). https://doi.org/10.1016/j.engstruct.2021.111858.

[30] Z. Dai, S.D. Pang, J.Y.R. Liew, Axial load resistance of grouted sleeve connection for modular construction, Thin-Walled Struct. 154 (2020) 106883. https://doi.org/10.1016/j.tws.2020.106883.

[31] J. Peng, C. Hou, L. Shen, Progressive collapse analysis of corner-supported composite modular buildings, J. Build. Eng. 48 (2022) 103977. https://doi.org/10.1016/j.jobe.2021.103977.

[32] Z. Chen, J. Wang, J. Liu, K. Khan, Seismic behavior and moment transfer capacity of an innovative self-locking inter-module connection for modular steel building, Eng. Struct. 245 (2021) 112978. https://doi.org/10.1016/j.engstruct.2021.112978.

[33] X. Dai, L. Zong, Y. Ding, Z. Li, Experimental study on seismic behavior of a novel plug-in self-lock joint for modular steel construction, Eng. Struct. 181 (2019) 143–164. https://doi.org/10.1016/j.engstruct.2018.11.075.

[34] S. Srisangeerthanan, M.J. Hashemi, P. Rajeev, E. Gad, S. Fernando, Development of an Innovative Boltless Connection for Multistory Modular Buildings, J. Struct. Eng. 148 (2022) 1–19. https://doi.org/10.1061/(ASCE)ST.1943-541X.0003382.

[35] G. Nadeem, N. Azizi, N. Abu, I. Abd, Experimental and numerical study of self-locking adaptable inter connection for modular steel structures, J. Build. Eng. 65 (2023) 105723. https://doi.org/10.1016/j.jobe.2022.105723.

[36] R. Sanches, O. Mercan, B. Roberts, Experimental investigations of vertical post-tensioned connection for modular steel structures, Eng. Struct. 175 (2018) 776–789. https://doi.org/10.1016/j.engstruct.2018.08.049.

[37] A.W. Lacey, W. Chen, H. Hao, K. Bi, New interlocking inter-module connection for modular steel buildings : Experimental and numerical studies, Eng. Struct. 198 (2019) 109465. https://doi.org/10.1016/j.engstruct.2019.109465.

[38] J.Y.R. Liew, Y.S. Chua, Z. Dai, Steel concrete composite systems for modular construction of high-rise buildings, Structures. 21 (2019) 135–149. https://doi.org/10.1016/j.istruc.2019.02.010.

[39] Z. Chen, H. Li, A. Chen, Y. Yu, H. Wang, Research on pretensioned modular frame test and simulations, Eng. Struct. 151 (2017) 774–787. https://doi.org/10.1016/j.engstruct.2017.08.019.

[40] Z. Chen, J. Wang, J. Liu, Z. Cong, Tensile and shear performance of rotary inter-module connection for modular steel buildings, J. Constr. Steel Res. 175 (2020) 106367. https://doi.org/10.1016/j.jcsr.2020.106367.

[41] F. Shi, Y. Ding, L. Zong, Y. Chen, Y. Wu, Shear behaviour of vertical inter-module connection with bolts and shear keys for MSCs, Structures. 47 (2023) 260–281. https://doi.org/10.1016/j.istruc.2022.11.046.

[42] G. Nadeem, N. Azizi, N. Abu, I. Abd, Evaluation of slip behaviour of self-locking modular steel connection, J. Constr. Steel Res. 197 (2022) 107467. https://doi.org/10.1016/j.jcsr.2022.107467.

[43] F. Shi, Y. Ding, L. Zong, X. Meng, Y. Chen, Axial mechanical behavior of innovative inter-module connection for modular steel constructions, J. Build. Eng. 65 (2023) 105765. https://doi.org/10.1016/j.jobe.2022.105765.

[44] J. Doh, N.M. Ho, D. Miller, T. Peters, D. Carlson, P. La, Steel Bracket Connection on Modular Buildings, J. Steel Struct. Constr. (2016). https://doi.org/10.4172/2472-0437.1000121.

[45] Y. Yu, Z. Chen, A. Chen, Experimental study of a pretensioned connection for modular buildings, Steel Compos. Struct. 31 (2019) 217–232. https://doi.org/10.12989/scs.2019.31.3.217.

[46] Z. Chen, J. Liu, Y. Yu, Experimental study on interior connections in modular steel buildings, Eng. Struct. 147 (2017) 625–638. https://doi.org/10.1016/j.engstruct.2017.06.002.

[47] E. Deng, L. Zong, Y. Ding, X. Dai, N. Lou, Y. Chen, Monotonic and cyclic response of bolted connections with welded cover plate for modular steel construction, Eng. Struct. 167 (2018) 407–419. https://doi.org/10.1016/j.engstruct.2018.04.028.

[48] Z. Chen, J. Liu, Y. Yu, C. Zhou, R. Yan, Experimental study of an innovative modular steel building connection, J. Constr. Steel Res. 139 (2017) 69–82. https://doi.org/10.1016/j.jcsr.2017.09.008.

[49] M. Farajian, P. Sharafi, K. Kildashti, The influence of inter-module connections on the effective length of columns in multi-story modular steel frames, J. Constr. Steel Res. 177 (2021). https://doi.org/10.1016/j.jcsr.2020.106450.

[50] L. Huan, Y. Yong, Y. Deng, Study on influence of width-to-thickness ratios on static performance of the thin-wall square steel tube columns to axial loads, Build. Sci. 29 (2013).

[51] S.D. Nie, S.B. Kang, L. Shen, B. Yang, Experimental and numerical study on global buckling of Q460GJ steel box columns under eccentric compression, Eng. Struct. 142 (2017) 211–222. https://doi.org/10.1016/j.engstruct.2017.03.064.

[52] D.C. Fratamico, S. Torabian, X. Zhao, K.J.R. Rasmussen, B.W. Schafer, Experiments on the global buckling and collapse of built-up cold-formed steel columns, J. Constr. Steel Res. 144 (2018) 65–80. https://doi.org/10.1016/j.jcsr.2018.01.007.

[53] X. Zheng, Y. Zou, B. He, J. Xiang, Z. Li, Q. Yang, Buckling Analysis and Structure Improvement

for the Afterburner Cylinder of an Aero-Engine, Aerospace. 10 (2023). https://doi.org/10.3390/aerospace10050484.

[54] IS 801 - 1975, Indian Standard code of practice for use of cold-formed light gauge steel structural members in general building construction, (1975).

[55] IS:800, Indian standard code of practice for general construction in steel, Bur. Indian Stand. New Delhi. (2007).

[56] NZS3404, Part 1:1997-Steel Structures Standard, (1997).

[57] EN 1993-1-1, Eurocode 3: Design of steel structures - Part 1-1: General rules and rules for buildings, 2005.

[58] CSA-S16-09, CSA standard-Design of steel structures, 2009.

[59] ANSI/AISC 360-16, AISC360/16 Specification for Structural Steel Buildings-An American National Standard, 2016.

[60] GB50017-2017, Standard for design of steel structures (in Chinese), (2017).

[61] CISC, CISC Code of Standard Practice for structural steel, 2016.

[62] JGJ, Technical specification for steel structure of tall building (in Chinese), 2016.

[63] Q. Wang, M. Su, Stability study on sway modular steel structures with semi-rigid connections, Thin-Walled Struct. 161 (2021). https://doi.org/10.1016/j.tws.2021.107529.

[64] R. Mark Lawson, J. Richards, Modular design for high-rise buildings, Proc. Inst. Civ. Eng. Struct. Build. 163 (2010) 151–164. https://doi.org/10.1680/stbu.2010.163.3.151.

[65] J.D. Aristizabal-Ochoa, Stability of multi-column systems with initial imperfections and non-linear connections, Int. J. Non. Linear. Mech. 57 (2013) 75–89. https://doi.org/10.1016/j.ijnonlinmec.2013.06.012.

[66] K. Khan, Z. Chen, J. Liu, A. Khan, K. Javed, Axial compression behaviours of tubular sectioned C-shape continuous-supported steel walls in MSB, J. Constr. Steel Res. 188 (2022) 107009. https://doi.org/10.1016/j.jcsr.2021.107009.

[67] K. Khan, Z. Chen, J. Liu, A. Khan, Numerical and parametric analysis on compressive behaviours of continuous-supported wall systems in MSB, Structures. 33 (2021) 4053–4079. https://doi.org/10.1016/j.istruc.2021.07.001.

[68] K. Khan, Z. Chen, J. Liu, A. Khan, Experimental and numerical study on planar multi-column walls behaviours with boundary supports, J. Constr. Steel Res. 186 (2021) 106880. https://doi.org/10.1016/j.jcsr.2021.106880.

[69] E.F. Deng, J.B. Yan, Y. Ding, L. Zong, Z.X. Li, X.M. Dai, Analytical and numerical studies on steel columns with novel connections in modular construction, Int. J. Steel Struct. 17 (2017) 1613–1626. https://doi.org/10.1007/s13296-017-1226-5.

[70] Y. Chen, C. Hou, J. Peng, Stability study on tenon-connected SHS and CFST columns in modular construction, Steel Compos. Struct. 30 (2019) 185–199. https://doi.org/10.12989/scs.2019.30.2.185.

[71] K. Khan, Z. Chen, J. Liu, K. Javed, Experimental and analytical investigations on compressive behaviors of modular steel shear-keyed tubes, Eng. Struct. 279 (2023) 115604. https://doi.org/10.1016/j.engstruct.2023.115604.

[72] K. Khan, Z. Chen, J. Liu, K. Javed, Compressive behaviors of modular steel shear-keyed grouped tubular columns, J. Build. Eng. 66 (2023) 105861. https://doi.org/10.1016/j.jobe.2023.105861.

[73] K. Khan, Z. Chen, J. Liu, K.D. Tsavdaridis, K. Poologanathan, Axial compression behaviors of steel shear-keyed tubular columns: Numerical and analytical studies, J. Constr. Steel Res. (2023).

[74] Z. Pengfei, Z. Xizhi, C. Zhihua, Z. Tianxin, Design and Mechanical Properties of Multi-storey Steel Module Structure (in Chinese), Tianjin University, 2015.

[75] G.Q. Li, K. Cao, Y. Lu, J. Jiang, Effective length factor of columns in non-sway modular steel buildings, Adv. Steel Constr. 13 (2017) 412–426. https://doi.org/10.18057/IJASC.2017.13.4.6.

[76] G.Q. Li, K. Cao, Y. Lu, Column effective lengths in sway-permitted modular steel-frame buildings, Proc. Inst. Civ. Eng. Struct. Build. 172 (2019) 30–41.

https://doi.org/10.1680/jstbu.17.00006.

[77] X. Zhai, X. Zha, D. Chen, Elastic stability of unbraced plate-type modular steel frames with semi-rigid corner connections, J. Constr. Steel Res. 192 (2022) 107243. https://doi.org/10.1016/j.jcsr.2022.107243.

[78] Q. Wang, M. Su, Stability study on sway modular steel structures with semi-rigid connections, Thin-Walled Struct. 161 (2021) 107529. https://doi.org/10.1016/j.tws.2021.107529.

[79] P. Dumonteil, Simple Equations for Effective Length Factors, Am. Inst. Steel Constr. Vol. 29 (1992) 111–115.

[80] M. Farajian, P. Sharafi, H. Eslamnia, Y. Bai, B. Samali, Classification system for inter-modular connections in non-sway corner-supported steel modular buildings, Structures. 49 (2023) 807–825. https://doi.org/10.1016/j.istruc.2023.01.152.

[81] M. Farajian, P. Sharafi, H. Eslamnia, K. Kildashti, Y. Bai, Classification of inter-modular connections for stiffness and strength in sway corner-supported steel modular frames, J. Constr. Steel Res. 107458 (2022).

[82] X.H.C. He, T.M. Chan, Classification system for inter- and intra-module joints in non-sway steel MiC structures, J. Constr. Steel Res. 206 (2023) 107913. https://doi.org/10.1016/j.jcsr.2023.107913.

[83] Z. Chen, X. Zhong, Y. Liu, J. Liu, Analytical and Design Method for the Global Stability of Modular Steel Buildings, Int. J. Steel Struct. 21 (2021) 1741–1758. https://doi.org/10.1007/s13296-021-00532-8.

[84] P. Sharafi, M. Mortazavi, B. Samali, H. Ronagh, Interlocking system for enhancing the integrity of multi-storey modular buildings, Autom. Constr. 85 (2018) 263–272. https://doi.org/10.1016/j.autcon.2017.10.023.

[85] B. Xu, J. Xia, H. Chang, R. Ma, L. Zhang, A comprehensive experimental-numerical investigation on the bending response of laminated double channel beams in modular buildings, Eng. Struct. 200 (2019). https://doi.org/10.1016/j.engstruct.2019.109737.

[86] B. Xu, J. Xia, H. Chang, R. Ma, L. Zhang, Evaluation of superimposed bending behaviour of laminated channel beams in modular steel buildings subjected to lateral load, Thin-Walled Struct. J. 175 (2022). https://doi.org/10.1016/j.tws.2022.109234.

[87] R. Ma, J. Xia, H. Chang, B. Xu, L. Zhang, Experimental and numerical investigation of mechanical properties on novel modular connections with superimposed beams, Eng. Struct. 232 (2021). https://doi.org/10.1016/j.engstruct.2021.111858.

[88] A.W. Lacey, W. Chen, H. Hao, Experimental methods for inter-module joints in modular building structures – A state-of-the-art review, J. Build. Eng. 46 (2022) 103792. https://doi.org/10.1016/j.jobe.2021.103792.

[89] Y. Liu, Z. Chen, J. Liu, X. Zhong, X. Liu, J. Jiang, Effects of various reinforcing intra-module connection details on seismic behavior of corner-supported steel modular buildings, Structures. 40 (2022) 555–570. https://doi.org/10.1016/j.istruc.2022.04.041.

[90] X. Zhong, Z. Chen, J. Liu, Y. Liu, X. Liu, Experimental research on the in-plane performance of discontinuous modular diaphragms, Thin-Walled Struct. 173 (2022) 108905. https://doi.org/10.1016/j.tws.2022.108905.

[91] R. Sanches, O. Mercan, Vertical post-tensioned connection for modular steel buildings, in: 12th Can. Conf. Earthq. Eng. Quebec City, 2019: pp. 1–8.

[92] GB/T 228.1-2010, Metallic materials-Tensile testing-Part 1: Method of test at room temperature (in Chinese), (2010).

[93] Y. Liu, Z. Chen, J. Liu, X. Zhong, X. Liu, J. Jiang, Effects of various reinforcing intra-module connection details on seismic behavior of corner-supported steel modular buildings, Structures. 40 (2022) 555–570. https://doi.org/10.1016/j.istruc.2022.04.041.

[94] GBT50344-2019, Technical standards for building structure inspection (in Chinese), (2019).

[95] Y. Yu, L. Lan, Z. Chen, J. Huang, Mechanical and seismic behaviors of bottom-flange-bolted upper-flange-welded through-diaphragm connections, J. Constr. Steel Res. 156 (2019) 86–95.

https://doi.org/10.1016/j.jcsr.2019.01.015.

[96] J.B. Yan, X. Dong, J.S. Zhu, Behaviours of stub steel tubular columns subjected to axial compression at low temperatures, Constr. Build. Mater. 228 (2019) 116788. https://doi.org/10.1016/j.conbuildmat.2019.116788.

[97] S.B. Kang, B. Yang, X. Zhou, S.D. Nie, Global buckling behaviour of welded Q460GJ steel box columns under axial compression, J. Constr. Steel Res. 140 (2018) 153–162. https://doi.org/10.1016/j.jcsr.2017.10.013.

[98] S. Kazemzadeh Azad, D. Li, B. Uy, Axial slenderness limits for duplex and lean duplex stainless steel-concrete composite columns, J. Constr. Steel Res. 172 (2020) 106175. https://doi.org/10.1016/j.jcsr.2020.106175.

[99] Y. Du, M. Fu, Z. Chen, J. Yan, Z. Zheng, Axial compressive behavior of CFRP confined rectangular CFT columns using high-strength materials : Numerical analysis and carrying capacity model, Structures. 36 (2022) 997–1020. https://doi.org/10.1016/j.istruc.2021.12.061.

[100] J. Yan, J. Feng, Y. Luo, Y. Du, Compression behaviour of stainless-steel stub square tubular columns at cold-region low temperatures, J. Constr. Steel Res. 187 (2021) 106984. https://doi.org/10.1016/j.jcsr.2021.106984.

[101] J. Yan, B. Zhang, X. Yu, J. Xie, Thin-Walled Structures Mechanical properties of stainless steel QN1906Mo at sub-zero temperatures : Tests and stress – strain models, Thin-Walled Struct. 179 (2022) 109727. https://doi.org/10.1016/j.tws.2022.109727.

[102] J.B. Yan, Y.L. Luo, C. Liang, X. Lin, Y.B. Luo, L. Zhang, Compression behaviours of concrete-filled Q690 high-strength steel tubular columns at low temperatures, J. Constr. Steel Res. 187 (2021) 106983. https://doi.org/10.1016/j.jcsr.2021.106983.

[103] J.B. Yan, X. Yang, Y. Luo, P. Xie, Y.B. Luo, Axial compression behaviours of ultra-high performance concrete-filled Q690 high-strength steel tubes at low temperatures, Thin-Walled Struct. 169 (2021) 108419. https://doi.org/10.1016/j.tws.2021.108419.

[104] J.B. Yan, T. Wang, X. Dong, Compressive behaviours of circular concrete-filled steel tubes exposed to low-temperature environment, Constr. Build. Mater. 245 (2020) 118460. https://doi.org/10.1016/j.conbuildmat.2020.118460.

[105] J.B. Yan, W.J. Xie, Y. Luo, T. Wang, Behaviours of concrete stub columns confined by steel tubes at cold-region low temperatures, J. Constr. Steel Res. 170 (2020) 106124. https://doi.org/10.1016/j.jcsr.2020.106124.

[106] J.B. Yan, X. Dong, T. Wang, Axial compressive behaviours of square CFST stub columns at low temperatures, J. Constr. Steel Res. 164 (2020) 105812. https://doi.org/10.1016/j.jcsr.2019.105812.

[107] J.B. Yan, Y.L. Luo, L. Su, X. Lin, Y.B. Luo, L. Zhang, Low-temperature compression behaviour of square CFST columns using Q960 ultra-high strength steel, J. Constr. Steel Res. 183 (2021). https://doi.org/10.1016/j.jcsr.2021.106727.

[108] ABAQUS (2013), User manual Version 6.13., DS SIMULIA Corp, Provid. RI, USA. (2013) 1–847.

[109] K. Khan, J.-B. Yan, Finite Element Analysis on Seismic Behaviour of Novel Joint in Prefabricated Modular Steel Building, Int. J. Steel Struct. 20 (2020). https://doi.org/10.1007/s13296-020-00320-w.

[110] J. Peng, C. Hou, L. Shen, Numerical analysis of corner-supported composite modular buildings under wind actions, J. Constr. Steel Res. 187 (2021) 106942. https://doi.org/10.1016/j.jcsr.2021.106942.

[111] J. Peng, C. Hou, L. Shen, Numerical simulation of weld fracture using cohesive interface for novel inter-module connections, J. Constr. Steel Res. 174 (2020) 106302. https://doi.org/10.1016/j.jcsr.2020.106302.

[112] J. Peng, C. Hou, L. Shen, Lateral resistance of multi-story modular buildings using tenon-connected inter-module connections, J. Constr. Steel Res. 177 (2021) 106453. https://doi.org/10.1016/j.jcsr.2020.106453.

[113] K. Khan, J. Yan, Numerical studies on the seismic behaviour of a prefabricated multi-storey

modular steel building with new-type bolted joints, Adv. Steel Constr. 17 (2021) 1–9. https://doi.org/10.18057/IJASC.2021.17.1.1.

[114] K. Khan, Z. Chen, J. Liu, J. Yan, Simplified modelling of novel non-welded joints for modular steel buildings, Adv. Steel Constr. 17 (2021) 412–424. https://doi.org/10.18057/IJASC.2021.17.4.10.

[115] L. Jia, Y. Zhao, H. Liu, Z. Chen, K. Kashan, Flexural performance of weld-strengthened steel beam-square column joints subjected to axial column loading, J. Constr. Steel Res. 199 (2022) 107599. https://doi.org/10.1016/j.jcsr.2022.107599.

[116] L. Gardner, N. Saari, F. Wang, Comparative experimental study of hot-rolled and cold-formed rectangular hollow sections, Thin-Walled Struct. 48 (2010) 495–507. https://doi.org/10.1016/j.tws.2010.02.003.

[117] I. Arrayago, K.J.R. Rasmussen, Influence of the imperfection direction on the ultimate response of steel frames in advanced analysis, J. Constr. Steel Res. 190 (2022) 107137. https://doi.org/10.1016/j.jcsr.2022.107137.

[118] M. Theofanous, L. Gardner, Testing and numerical modelling of lean duplex stainless steel hollow section columns, Eng. Struct. 31 (2009) 3047–3058. https://doi.org/10.1016/j.engstruct.2009.08.004.

[119] J.B. Yan, X. Dong, J.S. Zhu, Behaviours of stub steel tubular columns subjected to axial compression at low temperatures, Constr. Build. Mater. 228 (2019). https://doi.org/10.1016/j.conbuildmat.2019.116788.

[120] J.B. Yan, J. Feng, Y.B. Luo, Y. Du, Compression behaviour of stainless-steel stub square tubular columns at cold-region low temperatures, J. Constr. Steel Res. 187 (2021) 106984. https://doi.org/10.1016/j.jcsr.2021.106984.

[121] J.-H. Zhu, B. Young, Cold-Formed-Steel Oval Hollow Sections under Axial Compression, J. Struct. Eng. 137 (2011) 719–727. https://doi.org/10.1061/(asce)st.1943-541x.0000337.

[122] M.A. Dabaon, M.H. El-Boghdadi, M.F. Hassanein, A comparative experimental study between stiffened and unstiffened stainless steel hollow tubular stub columns, Thin-Walled Struct. 47 (2009) 73–81. https://doi.org/10.1016/j.tws.2008.05.008.

[123] J.B. Yan, Y. Geng, Y. Luo, B. Zhao, T. Wang, Double skin composite beams at Arctic low temperatures: Numerical and analytical studies, J. Constr. Steel Res. 193 (2022) 107286. https://doi.org/10.1016/j.jcsr.2022.107286.

[124] W.F. Chen, E.M. Lui, Stability design of steel frames, CRC Press, 1991.